Cancer Cell

Article

Distinct roles of TREM2 in central nervous system cancers and peripheral cancers

Graphical abstract

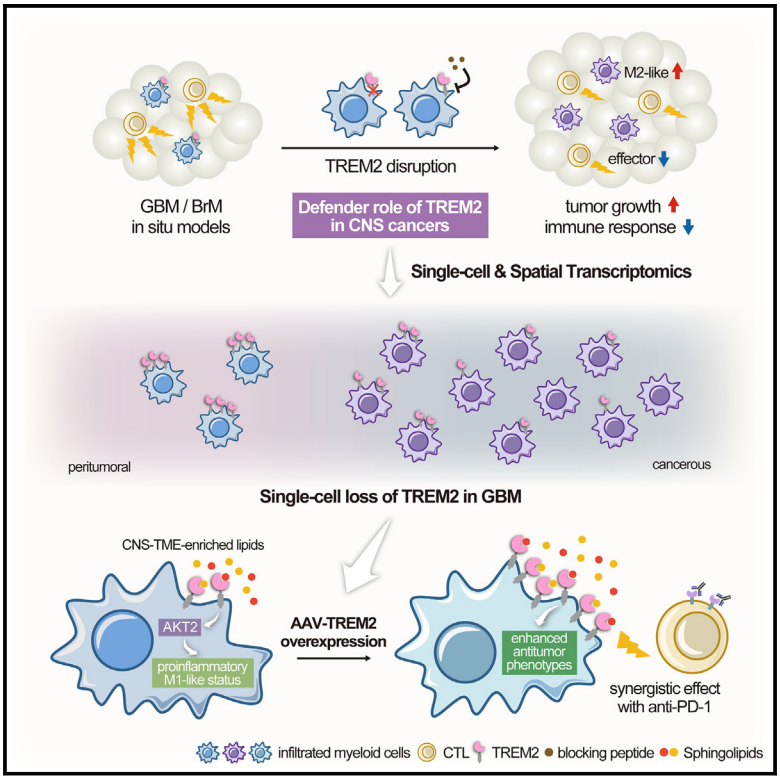

Highlights

- TREM2 deficiency promotes tumor progression in murine glioblastoma (GBM) models
- TREM2 downregulation is observed in individual GBM-infiltrated myeloid cells
- AAV-mediated TREM2 overexpression represses GBM growth and synergizes with ICB
- Lipidic damage signals causes a TREM2-mediated protective response in CNS cancers

Authors

Jian Zhong, Xudong Xing, Yixin Gao, ..., Yu Shi, Fan Bai, Nu Zhang

Correspondence

fbai@pku.edu.cn (F.B.),
zhangnu2@mail.sysu.edu.cn (N.Z.)

In brief

Zhong et al. show that TREM2 plays an immunoprotective role prompted by central nervous system-enriched sphingolipids during glioblastoma (GBM) progression. Single-cell and spatial sequencing revealed TREM2 downregulation in GBM-infiltrating myeloid cells. TREM2 overexpression represses GBM and synergizes with anti-PD-1 therapy. This study highlights organ-specific remodeling of myeloid cell targets in cancer immunotherapy.

Zhong et al., 2024, Cancer Cell *42*, 1–17
June 10, 2024
https://doi.org/10.1016/j.ccell.2024.05.001

CellPress

Please cite this article in press as: Zhong et al., Distinct roles of TREM2 in central nervous system cancers and peripheral cancers, Cancer Cell (2024), https://doi.org/10.1016/j.ccell.2024.05.001

Cancer Cell

CellPress

Article

Distinct roles of TREM2 in central nervous system cancers and peripheral cancers

Jian Zhong,[1,2,9] Xudong Xing,[3,4,9] Yixin Gao,[1,2,9] Lei Pei,[3,4] Chenfei Lu,[5] Huixin Sun,[1,2] Yanxing Lai,[1,2] Kang Du,[1,2] Feizhe Xiao,[6] Ying Yang,[7,8] Xiuxing Wang,[5] Yu Shi,[7,8] Fan Bai,[3,4,*] and Nu Zhang[1,2,10,*]

[1]Department of Neurosurgery, The First Affiliated Hospital of Sun Yat-sen University, Guangzhou, Guangdong 510080, China
[2]Guangdong Provincial Key Laboratory of Brain Function and Disease, Guangzhou, Guangdong 510080, China
[3]Biomedical Pioneering Innovation Center (BIOPIC), Peking-Tsinghua Center for Life Sciences, School of Life Sciences, Peking University, Beijing, China
[4]Beijing Advanced Innovation Center for Genomics, Peking University, Beijing, China
[5]Department of Cell Biology, National Health Commission Key Laboratory of Antibody Techniques, School of Basic Medical Sciences, Nanjing Medical University, Nanjing, Jiangsu 211166, China
[6]Department of Scientific Research Section, The First Affiliated Hospital of Sun Yat-sen University, Guangzhou, Guangdong 510080, China
[7]Institute of Pathology and Southwest Cancer Centre, Key Laboratory of Tumor Immunopathology of the Ministry of Education of China, Southwest Hospital, Third Military Medical University (Army Medical University), Chongqing 400038, China
[8]Yu-Yue Pathology Scientific Research Center and Jinfeng Laboratory, Chongqing 400039, China
[9]These authors contributed equally
[10]Lead contact
*Correspondence: fbai@pku.edu.cn (F.B.), zhangnu2@mail.sysu.edu.cn (N.Z.)
https://doi.org/10.1016/j.ccell.2024.05.001

SUMMARY

Glioblastomas (GBM) are incurable central nervous system (CNS) cancers characterized by substantial myeloid cell infiltration. Whether myeloid cell-directed therapeutic targets identified in peripheral non-CNS cancers are applicable to GBM requires further study. Here, we identify that the critical immunosuppressive target in peripheral cancers, triggering receptor expressed on myeloid cells-2 (TREM2), is immunoprotective in GBM. Genetic or pharmacological TREM2 deficiency promotes GBM progression *in vivo*. Single-cell and spatial sequencing reveals downregulated TREM2 in GBM-infiltrated myeloid cells. TREM2 negatively correlates with immunosuppressive myeloid and T cell exhaustion signatures in GBM. We further demonstrate that during GBM progression, CNS-enriched sphingolipids bind TREM2 on myeloid cells and elicit antitumor responses. Clinically, high TREM2 expression in myeloid cells correlates with better survival in GBM. Adeno-associated virus-mediated TREM2 overexpression impedes GBM progression and synergizes with anti-PD-1 therapy. Our results reveal distinct functions of TREM2 in CNS cancers and support organ-specific myeloid cell remodeling in cancer immunotherapy.

INTRODUCTION

Triggering receptor expressed on myeloid cells-2 (TREM2), a myeloid cell surface receptor, is a major immune signaling hub in various diseases.[1] Physiologically, TREM2 is expressed in a limited number of tissue-specific myeloid cells, including microglia (MG) in the central nervous system (CNS), to maintain cellular homeostasis.[1] In pathological conditions, TREM2 binds to many ligands released from the lesion sites, and the TREM2 pathway becomes central for sensing damage and restricting its spread.[2–5] In Alzheimer's disease (AD), TREM2-deficient mice show impaired MG function and Aβ plaque aggregation.[3] The R47H mutation in TREM2, which disrupts TREM2 ligand binding ability, is a confirmed AD risk factor in humans.[3,6]

However, the role of TREM2 in cancer is more complicated. Accumulating evidence suggests that TREM2 expression is limited to tumor-associated macrophages (TAMs) and myeloid-derived suppressor cells (MDSCs).[7] The combination of anti-TREM2 and anti-PD-1 antibodies showed promising effects in several different cancers, including sarcoma, colorectal, and breast cancers.[8] In hepatocellular carcinoma, whether TREM2 is tumor-promotive or tumor-suppressive is controversial.[9,10] These different roles of TREM2 may result from the diversity of its ligands and subsequent intracellular signaling transduction mechanisms mediated by DAP10/12, which may exert opposing downstream effects depending on the tissue type and status.[2,11] Given its role in sensing environmental cues and eliciting diverse downstream signaling, TREM2 may be critical in the functional reprogramming of TAMs. However, the underlying mechanism whereby TREM2 redirects TAMs to an immunosuppressor or defender state has yet to be elucidated. How to utilize TREM2 to target TAMs or induce their reprogramming in different malignancies requires further study.

Please cite this article in press as: Zhong et al., Distinct roles of TREM2 in central nervous system cancers and peripheral cancers, Cancer Cell (2024), https://doi.org/10.1016/j.ccell.2024.05.001

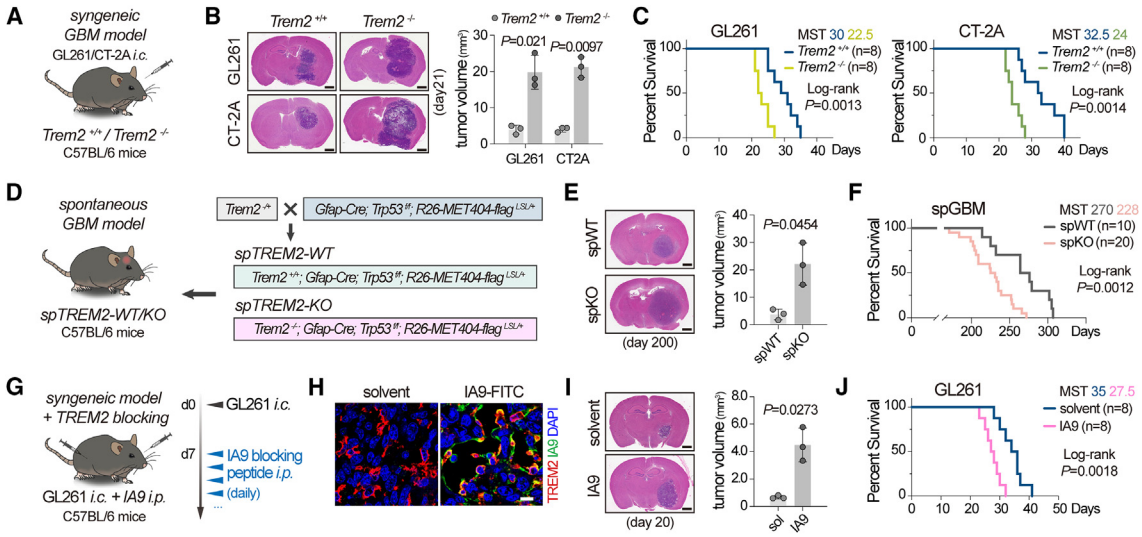

Figure 1. TREM2 deficiency promotes GBM progression in mice

(A) Illustration of the GL261/CT2A GBM model established in *Trem2*$^{+/+}$ and *Trem2*$^{-/-}$ mice. *i.c.*, intracranial injection.

(B) Left, representative hematoxylin and eosin (HE)-stained brain sections from GBM-bearing *Trem2*$^{+/+}$ and *Trem2*$^{-/-}$ mice. Scale bar, 1 mm. Right, quantification of tumor volume in the HE-stained brain sections (n = 3). Two-tailed paired t test.

(C) Kaplan-Meier analysis of GBM-bearing *Trem2*$^{+/+}$ and *Trem2*$^{-/-}$ mice (n = 8). MST, median survival time. Log rank test.

(D) Illustration of the crossing strategy for generating spTREM2-WT/KO mice.

(E) Left, representative HE-stained brain sections from spTREM2-WT/KO mice collected on day 200 after birth. Scale bar, 1 mm. Right, quantification of tumor volume in the HE-stained brain sections (n = 3). Two-tailed paired t test.

(F) Kaplan-Meier analysis of spTREM2-WT (n = 10) and spTREM2-KO (n = 20) mice. Log rank test.

(G) Illustration of GBM model mice treated with IA9. *i.p.*, intraperitoneal injection.

(H) Immunofluorescence staining of TREM2 and IA9-FITC in brain tumor sections from control or IA9-treated GL261-GBM-bearing mice. Scale bar, 10 μm.

(I) Left, representative HE-stained brain sections from control or IA9-treated mice. Scale bar, 1 mm. Right, quantification of tumor volume in the HE-stained brain sections (n = 3). Two-tailed paired t test.

(J) Kaplan-Meier analysis of control or IA9-treated GL261-GBM-bearing mice (n = 8 per group). Log rank test.

Data are represented as the mean ± SD in (B), (E), and (I).

See also Figure S1.

Glioblastoma (GBM), the most common and lethal primary CNS cancer, is characterized by considerable TAM infiltration (30%–50% of the cellular components).[12] TAMs in GBM are largely composed of resident MG and blood monocyte-derived macrophages (MDMs)[12] (hereon, "TAMs" refers to tumor-associated MG and MDMs in GBM, unless otherwise specified). Although TAMs have emerged as promising targets for immunotherapeutic intervention,[13] GBM showed unsatisfactory responses to TAM-targeted therapies compared with peripheral cancers in several clinical trials,[13–15] suggesting that GBM has a unique tumor microenvironment (TME) that shares few common characteristics with the TME of peripheral cancers.[16–19] Given the high heterogeneity of TAMs and other immune cells with sometimes opposing roles in GBM initiation, progression, and response to therapy,[20–23] recent studies applied single-cell RNA sequencing (scRNA-seq) to decipher the milieu and distinct TAM phenotypes in GBM.[24,25] Critical molecules governing TAM activities, including TGF-β in tumor-associated MG,[26,27] SDF-1/CXCR4 signaling in MDMs,[28] CSF-1 signaling,[29] CD39 and CD73 ectoenzymes,[30,31] and SIRPα-CD47 pathway,[32] are emerging as potential TAM targets. To date, therapeutic approaches have yet to be translated into clinical practice.[13–15,33] As a signaling hub on TAMs, the role of TREM2 in GBM and other CNS cancers is poorly understood, as single-cell analyses of TREM2 expression in GBM have rarely been reported. Clarifying the detailed role of TREM2 and its crosstalk with the TME in this lethal cancer is critical, as therapeutic strategies using TREM2 agonists or antibodies may be useful for the treatment of GBM and other CNS malignancies.

Here, we reveal the protective role of TREM2 in GBM and downregulation of TREM2 in infiltrated myeloid cells during GBM progression. Elevating TREM2 levels impedes GBM progression, highlighting the organ-specific remodeling of molecular targets in cancer immunotherapy.

RESULTS

TREM2 deficiency promotes GBM progression in mice

TREM2 is preferentially expressed in myeloid cells rather than other cell types[1] (Figures S1A–S1D). The Cancer Genome Atlas (TCGA) GBM dataset indicates overall TREM2 upregulation in tumors (Figure S1E). We thus genetically depleted TREM2 in C57BL/6 mice (*Trem2*$^{-/-}$ mice) (Figures S1F–S1H) to investigate its role in GBM. TREM2 depletion resulted in no gross abnormalities (e.g., unaffected survival)[34] or significant changes in the proportions of major immune cell populations (Figure S1I). Next, the mice were intracranially injected with murine syngeneic GBM cell lines (GL261 and CT-2A) (Figure 1A). Both implanted tumors

Please cite this article in press as: Zhong et al., Distinct roles of TREM2 in central nervous system cancers and peripheral cancers, Cancer Cell (2024), https://doi.org/10.1016/j.ccell.2024.05.001

CellPress

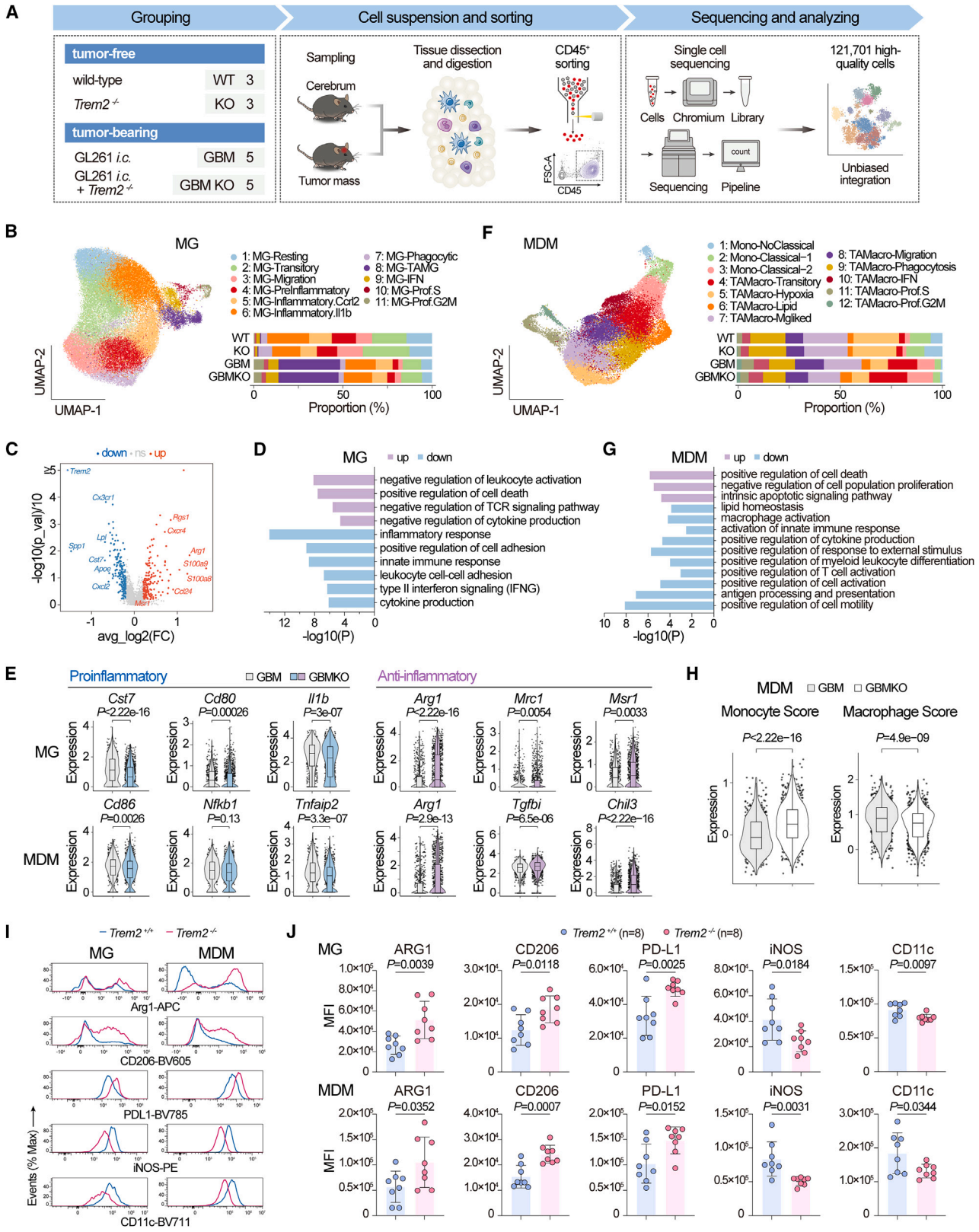

Figure 2. TREM2 deficiency induces an immunosuppressive TAM compartment in the GBM TME

(A) ScRNA-seq profiling workflow. WT, tumor-free *Trem2*$^{+/+}$ mice; KO, tumor-free *Trem2*$^{-/-}$ mice; GBM, GL261-GBM-bearing *Trem2*$^{+/+}$ mice; GBM KO, GL261-GBM-bearing *Trem2*$^{-/-}$ mice.

(legend continued on next page)

Please cite this article in press as: Zhong et al., Distinct roles of TREM2 in central nervous system cancers and peripheral cancers, Cancer Cell (2024), https://doi.org/10.1016/j.ccell.2024.05.001

grew significantly faster in *Trem2*$^{-/-}$ mice than in wild-type mice (Figure 1B). Shortened overall survival (OS) was also observed in the tumor-bearing *Trem2*$^{-/-}$ mice, as compared to the wild-type ones (Figure 1C).

To further validate the role of TREM2 in GBM, we crossed TREM2-deficient mice with spontaneous genetic GBM model mice[35] (*Gfap-Cre*; *Trp53*$^{f/f}$; *R26-MET404-flag*$^{LSL/+}$) and compared GBM growth in these mice (spTREM2-WT vs. spTREM2-KO) (Figures 1D and S1J). Consistent with aforementioned results, spTREM2-KO mice developed larger brain neoplasms than spTREM2-WT mice (Figure 1E), and the OS of the spTREM2-KO group was markedly shortened with the median survival time (MST) reduced by ~40 days (Figure 1F).

In addition, we employed a pharmacological TREM2-blocking model. GL261-GBM-bearing mice were administered with a TREM2 blocking peptide IA9[36] (Figure 1G). The injected peptide exerted minimal effects on peripheral immunity (Figures S1K and S1L), passed the blood-brain barrier and colocalized with TREM2 at the cell membrane in the TME (Figure 1H), and effectively blocked TREM2 downstream signaling in the sorted TAMs (Figure S1M). Consistently, IA9 treatment exacerbated tumor progression and shortened the OS (Figures 1I and 1J). The effect of IA9 was TREM2-dependent, as no differences in tumor growth and OS were observed between control or IA9-treated *Trem2*$^{-/-}$ mice (Figures S1N and S1O). In these TREM2-deficient mice, the cytotoxicity and cytokine production of CD8^{+} T cells and NK cells were not significantly affected by IA9 treatment (Figure S1P).

These data uncover a protective role for TREM2 against GBM progression, in contrast to its established tumor-promoting role in peripheral non-CNS cancers.[8,37,38]

TREM2 deficiency induces an immunosuppressive TAM compartment in the GBM TME

To understand the impact of TREM2 on the immune landscape during GBM progression, we employed scRNA-seq to analyze immune cells sorted from the normal brains or intracranial GL261 allografts collected from wild-type or *Trem2*$^{-/-}$ mice (Figure 2A, hereafter, tumor-free wild-type and *Trem2*$^{-/-}$ mice are referred as WT and KO; tumor-bearing wild-type and *Trem2*$^{-/-}$ mice are referred as GBM and GBM KO). A total of 121,701 cells were obtained. Unsupervised clustering by uniform manifold approximation and projection (UMAP) identified 12 cell types according to the expression of canonical gene markers (Figures S2A and S2B). *Ptprc* (CD45) expression was detected in most clusters, indicating trustworthy CD45^{+} sorting (Figure S2C). *Trem2* was expressed mainly in myeloid cells, including MG and macrophages (Figures S2D and S2E). Significantly reduced TREM2 expression levels were observed in the KO and GBM KO groups (Figures S2F and S2G), indicating effective TREM2 disruption in the *Trem2*$^{-/-}$ mouse model.

The proportion of identified cell types was not significantly changed after TREM2 depletion (WT vs. KO, GBM vs. GBM KO, Figures S2H and S2I) and was validated by flow cytometry (Figures S2J–S2L). TREM2 disruption only resulted in modest transcriptional changes in the tumor-free groups (WT vs. KO), whereas more remarkable transcriptional alterations were recorded in tumor-bearing groups (GBM vs. GBM KO) (Figure S2M), indicating critical functional involvement of TREM2 during GBM progression. Thus, we next focus on the role of TREM2 in shaping the TME of GBM (GBM vs. GBM KO).

We first concentrated on the two major infiltrated myeloid cell types (MG and MDMs) in GBM. Resident MG were reclustered into 11 subsets (Figures S2N and S2O), all of which highly expressed *Trem2* and exhibited successful TREM2 disruption in the KO group (Figures S2P and S2Q). We focused on a subset of cells only seen after tumor inoculation (TAMG, cluster 8). Although the proportion of this subset in the TME was similar between the GBM and GBM KO groups (Figures 2B and S2R), marked changes occurred at the transcriptional level, including a rise in *Arg1* (a hallmark of myeloid suppressive cells in the TME[39]) levels upon TREM2 disruption (Figure 2C; Table S1). Pathway analysis revealed significant negative regulation of leukocyte activation and cytokine production, indicating decreasing antitumor activities after TREM2 loss (Figure 2D). Several TREM2-associated genes (*Tyrobp*, *Apoe*, *Spp1*, and *Lpl*) were downregulated upon TREM2 depletion (Figure S2S), while similar patterns were observed in proinflammatory genes (*Cst7*, *Cd80*, and *Il1b*) (Figure 2E). In contrast, in addition to *Arg1*, other anti-inflammatory signatures (*Mrc1*, *Msr1*, *Ap1b1, Tgfbi*, and *Igf1*) were markedly upregulated in this TAMG cluster (Figures 2E and S2T).

The analysis was extended to other identified microglial subsets, yielding findings suggesting that TREM2 deficiency may potentially enhance the M2-like anti-inflammatory state while suppressing the M1-like proinflammatory state in MG, indicating a shift toward a more tumor-promoting status (Figure S2T).

(B) UMAP plot and bar graph showing identified cell clusters of MG and their proportion in the indicated groups.
(C) Volcano plot showing differentially expressed genes in the MG-TAMG cluster (GBM vs. GBM KO).
(D) Bar graph showing the functionally enriched pathways in the significantly upregulated or downregulated genes (GBM vs. GBM KO) in the MG (MG-TAMG) cluster.
(E) Violin-box plots showing the expression of proinflammatory or anti-inflammatory signatures in the MG (MG-TAMG) or the MDM (TAMacro-Lipid) clusters (GBM vs. GBM KO). Two-tailed unpaired Wilcoxon rank-sum test.
(F) UMAP plot and bar graph showing identified cell clusters of infiltrated MDMs and their proportion in the indicated groups.
(G) Bar graph showing the functionally enriched pathways in the significantly upregulated or downregulated genes (GBM vs. GBM KO) in the MDM (TAMacro-Lipid) cluster.
(H) Violin-box plots showing the monocyte or macrophage score of the MDM (TAMacro-Lipid) cluster (GBM vs. GBM KO). Two-tailed unpaired Wilcoxon rank-sum test.
(I and J) Representative histograms (I) and quantification (J, $n = 8$) showing the expression of M1-like or M2-like markers in MG or infiltrated MDMs from the indicated GBM model mice. Data are represented as the mean ± SD. Two-tailed unpaired t test.
For the violin-box plots in (E) and (H), the centerlines indicate the median. The box limits indicate the first and third quartiles. The whiskers indicate the maxima and minima.
See also Figures S2 and S3 and Tables S1 and S2.

Please cite this article in press as: Zhong et al., Distinct roles of TREM2 in central nervous system cancers and peripheral cancers, Cancer Cell (2024), https://doi.org/10.1016/j.ccell.2024.05.001

CellPress

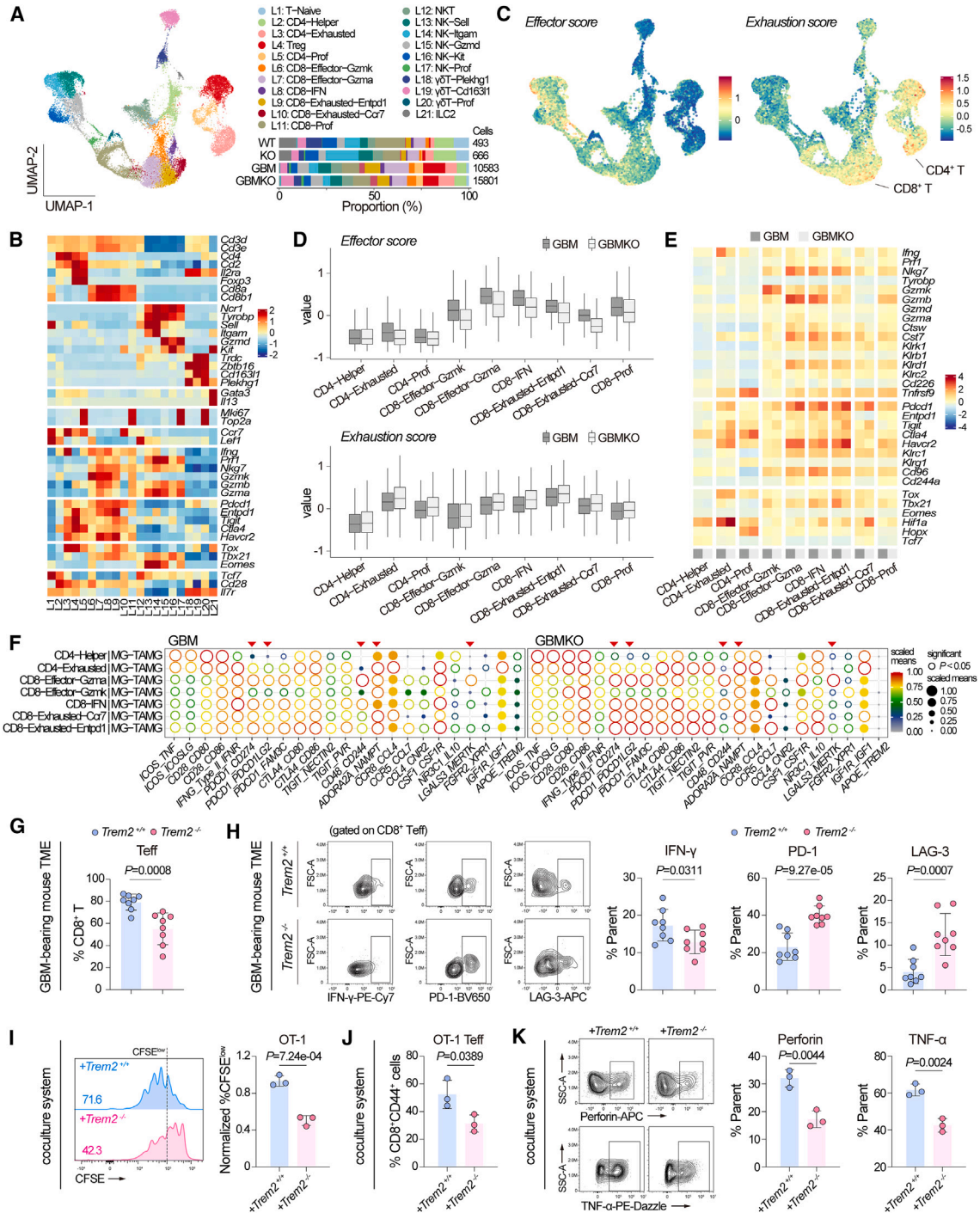

Figure 3. TREM2 deficiency in myeloid cells impairs T cell antitumor activity in GBM

(A) UMAP plot and bar plot showing the identified lymphoid subset clusters and their proportion in the indicated groups.

(B) Heatmap showing the expression levels of marker genes in the identified lymphoid clusters. Gene expression levels are color coded, ranging from blue (low expression levels) to red (high expression levels).

(C) The levels of effector (left) or exhaustion (right) scores of the identified lymphoid clusters are indicated by a color gradient, ranging from blue (low expression levels) to red (high expression levels).

(D) Boxplots showing the effector or exhaustion scores in indicated clusters (GBM vs. GBM KO). The centerlines indicate the median. The box limits indicate the first and third quartiles. The whiskers indicate the maxima and minima.

(E) Heatmap of functional gene sets in CD4$^+$/CD8$^+$ T clusters (GBM vs. GBM KO). Expression levels are color coded, ranging from blue (low expression levels) to red (high expression levels).

(legend continued on next page)

Please cite this article in press as: Zhong et al., Distinct roles of TREM2 in central nervous system cancers and peripheral cancers, Cancer Cell (2024), https://doi.org/10.1016/j.ccell.2024.05.001

Additionally, when MG were depleted before GBM inoculation without affecting peripheral blood and spleen myeloid cells[40] (Figures S2U–S2W), we observed no significant differences in tumor proliferation and mouse OS in our model (Figures S2X and S2Y). These results indicate that tumor-promotive and tumor-suppressive factors coexist in MG, while TREM2 represents a protective hub against GBM progression.

We next investigated the impact of TREM2 disruption on MDMs. We reclustered MDMs into 12 subclusters (Figures 2F, S3A, and S3B). *Trem2* disruption was observed in all subclusters and did not significantly affect the subcluster proportions (Figures S3C–S3E). We focused on the TAMacro-Lipid subset, which expressed the highest level of *Trem2* (Figure S3C). TREM2 disruption critically altered the expression of genes at the transcriptional level, marked by a pronounced increase in *Arg1* levels (Figure S3F; Table S2). The upregulated genes were enriched in the negative regulation of cell population proliferation and the intrinsic apoptotic signaling pathway, while the downregulated genes were enriched in macrophage activation and the positive regulation of T cell activation (Figure 2G). The expression of anti-inflammatory signatures (*Tgfbi* and *Chil3*) was upregulated, accompanied by downregulated proinflammatory signatures (*Cd86* and *Tnfaip2*) (Figure 2E). After TREM2 depletion, the monocyte signature score (*Ly6c2*, *Plac8*, *Ccr2*, *Gsr, Plaur*, etc.) was increased in this TAMacro-Lipid subset, along with a downregulation of macrophage signatures (*Apoe*, *C1qa*, *C1qb*, *C1qc*, *Ms4a7*, *Cd81*, *Egr1*, etc.) (Figure 2H), suggesting maturation arrest of macrophages in the TME of the TREM2-deficient group, which has been suggested to drive the insufficient activation of antitumor response.[39,41–43] The aforementioned results could largely be seen in the other identified macrophage subclusters (Figure S3G).

The enhanced anti-inflammatory and attenuated proinflammatory phenotypes of MG and MDMs were confirmed by flow cytometry using conventional markers (Figures 2I and 2J). The elevated expression of ARG1 was validated by the increased arginase activity in sorted GBM TAMs (Figure S3H). Additionally, given that phagocytic activity has been verified to participate in neoantigen presentation to cytotoxic T lymphocytes (CTL),[44] we evaluated the phagocytic activity of GBM TAMs upon TREM2 loss and revealed that significantly less bioparticles were phagocytized in TREM2-deficient TAMs (Figure S3I).

To further explore the role of TREM2 in MG and MDMs during GBM tumorigenesis, we established two mouse models. *Tmem119* and *Ccr2* are clustering markers good at distinguishing MG and MDMs[24,45–47] (Figures S2A and S2B). Two strains for TREM2 conditional knockout, $Tmem119^{CreER}$;$Trem2^{f/f}$ (MG-TREM2-CKO) and $Ccr2^{Cre}$;$Trem2^{f/f}$ (MDM-TREM2-CKO), were constructed (Figure S3J) and intracranially injected with GL261 or CT-2A GBM cells. The CKO control mice ($Trem2^{f/f}$ strain) exhibited no difference in tumor growth or OS when compared to the $Trem2^{+/+}$ control mice used in aforementioned results (Figures S3K–S3M). Both CKO strains showed faster tumor growth and a shorter OS, however, to a lesser extent when compared to the global TREM2 KO strain ($Trem2^{-/-}$ mice) (Figures S3K–S3M). These results further support that TREM2 expressed in MG and MDMs exhibits a protective role. A recent study highlights $TREM2^{+}$ neutrophils in prostate cancer patients.[37] However, little TREM2 expression in the neutrophils was observed in GBM (Figure S2E). Our data indicate that TREM2 exerts its protective effects mainly through MG and MDMs.

TREM2 deficiency in myeloid cells impairs T cell antitumor activity in GBM

Another indispensable component of the TME is the lymphoid subsets, of which $CD4^{+}$ helper T cells (Th) and $CD8^{+}$ CTLs are key players in the immune response against tumors. Since they dynamically interact with myeloid cells, we then asked whether TREM2 deficiency alters the T cell landscape. We reclustered the lymphoid compartment into 21 subsets (Figures 3A and 3B). TREM2 expression was barely detected in these subsets (Figures S4A and S4B). No significant proportional changes were observed in these subsets upon TREM2 disruption (WT vs. KO, GBM vs. GBM KO, Figure S4C). Compared to the homeostatic brain (WT), the TME of GBM consisted of decreased number of naive T cells and $CD4^{+}$ Th cells but an enlarged population of effector and exhausted $CD4^{+}$/$CD8^{+}$ T cells (Figure 3A). During GBM progression, the T cell subsets exhibited a phenotype characterized by effector-like signatures and marked exhaustion signatures (Figures 3C and S4D). ScRNA-seq profiling of immune cells from early stage and late-stage GBM samples also indicated concomitant activation and marked exhaustion of T cells during glioma progression (Figures S4E–S4I).

When we examined the effect of TREM2 loss on T cell subsets in the TME (GBM vs. GBM KO), we found that the cells of the TREM2-deficient group were characterized with downregulating effector score (*Gzmk*, *Gzmb*, *Cst7*, *Prf1*, etc.) and T helper score

(F) Bubble map showing the interactions of selected ligand-receptor pairs between $CD4^{+}$/$CD8^{+}$ T cells and the MG-TAMG subset. The scaled means of the average expression level of interacting molecule 1 in cluster 1 and interacting molecule 2 in cluster 2 are indicated by color gradients (blue, low level; red, high level) and circle size. Significant interactions ($p < 0.05$) are presented as a ring.

(G) Quantification of effector $CD8^{+}$ T cell ($CD44^{hi}CD62L^{lo}$) proportion in GBM-bearing $Trem2^{+/+}$ and $Trem2^{-/-}$ mice by flow cytometry ($n = 8$ per group). Two-tailed unpaired t test.

(H) Representative contour plots (left) and quantification (right) showing the proportion of effector $CD8^{+}$ T cells marked by IFN-γ and exhausted $CD8^{+}$ T cells marked by PD-1 and LAG-3 ($n = 8$ per group). Two-tailed unpaired t test.

(I) Representative histogram (left) and quantification (right) of proliferation ($CFSE^{low}$) of OT-1 cells after coculture with $OVA_{257-264}$-loaded $Trem2^{+/+}$ and $Trem2^{-/-}$ TAMs. $n = 3$ independent experiments. Two-tailed unpaired t test.

(J) Quantification of effector OT-1 cell ($CD62L^{lo}CD25^{+}$) proportion after coculture with $OVA_{257-264}$-loaded TAMs. $n = 3$ independent experiments. Two-tailed unpaired t test.

(K) Representative contour plots (left) and quantification (right) showing the proportions of perforin- or TNF-α-expressing OT-1 cells in the T cell priming assay. $n = 3$ independent experiments. Two-tailed unpaired t test.

Data are represented as the mean ± SD in (G–K).

See also Figure S4.

Please cite this article in press as: Zhong et al., Distinct roles of TREM2 in central nervous system cancers and peripheral cancers, Cancer Cell (2024), https://doi.org/10.1016/j.ccell.2024.05.001

CellPress

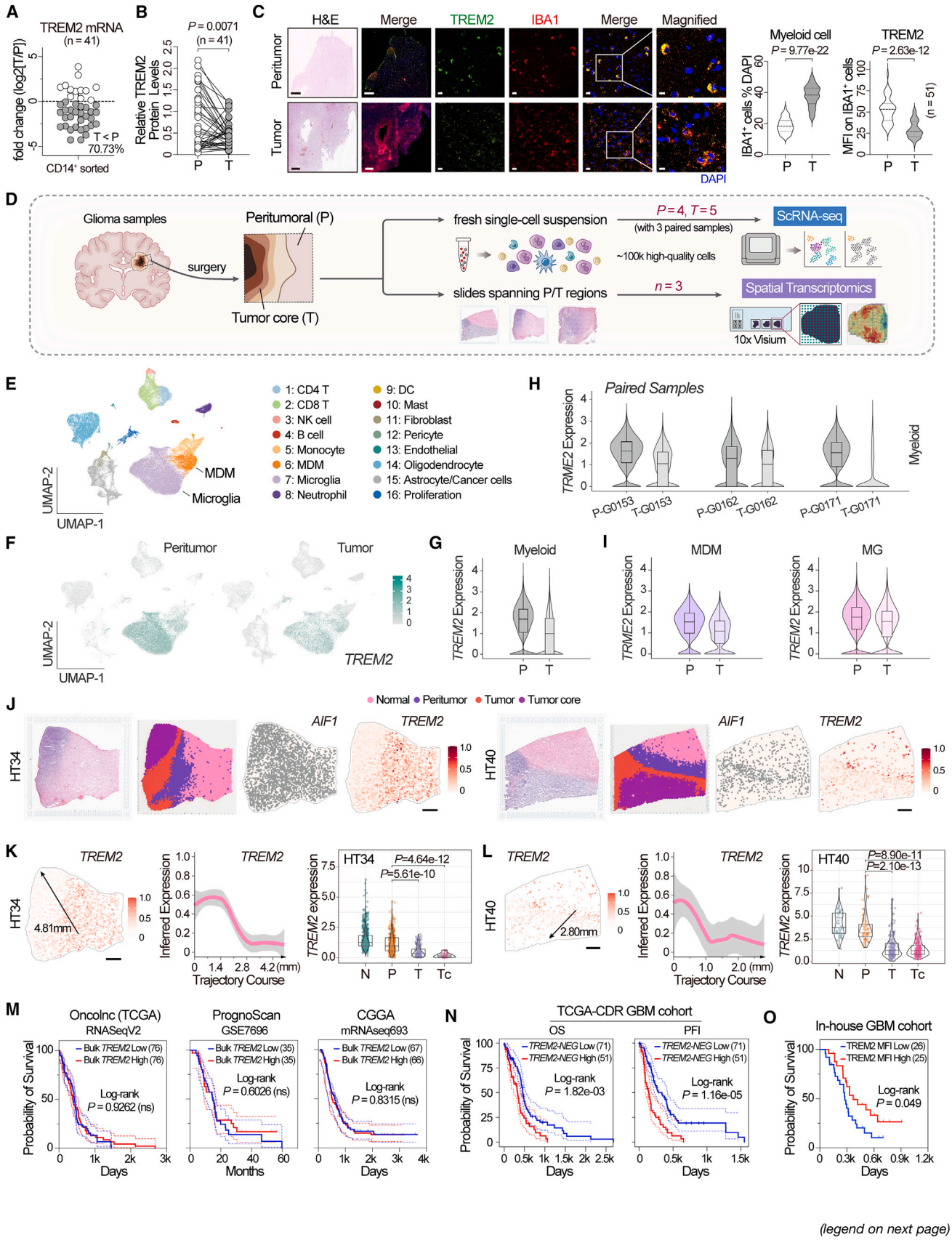

(legend on next page)

Please cite this article in press as: Zhong et al., Distinct roles of TREM2 in central nervous system cancers and peripheral cancers, Cancer Cell (2024), https://doi.org/10.1016/j.ccell.2024.05.001

(*Ifng*, *Tnf*, *Cd69*, *Il17a*, etc.) but further enhanced exhaustion score (*Pdcd1*, *Tigit*, *Ctla4*, etc.) (Figures 3D, 3E, and S4J), suggesting that TREM2 deficiency is responsible for the suppressed T cell activity against GBM. Differential gene expression analysis revealed that T cells in the TREM2-deficient group exhibited upregulated signatures of exhaustion (*Pdcd1*) and apoptosis (*Bcl2l11* and *Bcl2a1b*) and downregulated effector markers (*Gzmb*, *Prf1*, *Ifng*, and *Irf1*) (Figure S4K). Pathway analysis indicated that T cells in the TREM2-deficient group were enriched with upregulated checkpoint pathway, positive regulation of apoptotic process while with downregulated interferon signaling, adaptive immune response, and cell killing (Figure S4L).

Intercellular communication analysis indicated that TREM2 deficiency resulted in enhanced interaction between MG subsets and T cells that exhibited *PDCD1-CD274*, CD48-CD244, ADORA2A-NAMPT, and *LGASL3-MERTK* pairs, which were reported pairs involved in mediating the exhaustion of antitumor T cells[48–50] (Figures 3F and S4M). Flow cytometry profiling revealed decreased effector T cells ($CD44^{hi}CD62L^{lo}$) and IFN-$\gamma^{+}CD8^{+}$ T cells in the *Trem2*$^{-/-}$ TME, along with markedly increased exhausted $CD8^{+}$ T cells (PD-1^{+} and LAG-3^{+}) (Figures 3G and 3H).

To further validate that the TREM2 deficiency in GBM TAMs resulted in the observed phenotypes of CTLs, we sorted primary TAMs from *Trem2*$^{+/+}$ and *Trem2*$^{-/-}$ GL261-GBM-bearing mice and performed coculture assays with primary $CD8^{+}$ T cells. TREM2-deficient TAMs displayed upregulated activity in suppressing T cell activation when cocultured with polyclonal activated $CD8^{+}$ T cells in the T cell suppression assay (Figures S4N and S4O). In the antigen-specific T cell priming assay, TREM2-deficient TAMs were less proficient than wild-type TAMs (both loaded with $OVA_{257-264}$ peptide) in activating the naive OT-1 T cells, as indicated by decreased proliferation, effector proportion and effector marker (perforin/TNF-α) expression (Figures 3I–3K).

Overall, these results demonstrate that TREM2 deficiency in GBM TAMs results in a more immunosuppressive status and contributes to decreased CTL activity, thus leading to enhanced GBM progression.

Single-cell and spatial transcriptomics reveals TREM2 downregulation in myeloid components during GBM progression

GBM is reportedly capable of impairing extrinsic factors to establish an immunosuppressive TME that facilitates its progression.[17,21] Given the protective role of TREM2, we next wondered whether the endogenous TREM2 levels in myeloid cells are affected in GBM. We leveraged the scRNA-seq data to compare TREM2 expression between the tumor-bearing and tumor-free groups at the single-cell level (GBM vs. WT). In the GBM group, TREM2 expression was significantly downregulated in the whole myeloid cell compartment, MG and infiltrated MDMs (Figures S5A and S5B). These findings were validated in the peritumoral and cancerous tissues from the GL261-GBM-bearing mice by immunofluorescence (IF) (Figure S5C) and flow cytometry (Figure S5D).

Next, we asked whether this scenario occurs in human GBM. We first sorted myeloid cells ($CD14^{+}$) from paired GBM samples and subjected them to qPCR (Figure 4A) and immunoblot analysis (Figures 4B and S5E). Reduced TREM2 expression was observed

Figure 4. Single-cell and spatial transcriptomics reveals TREM2 downregulation in myeloid components during GBM progression

(A) Scatterplot showing the fold change in TREM2 mRNA levels in the sorted $CD14^{+}$ myeloid cells from tumoral tissues compared to those sorted from the peritumoral tissues. The gray dots indicate the samples with lower levels of TREM2 mRNA in tumoral $CD14^{+}$ cells compared to peritumoral ones. n = 41 independent paired human GBM samples. Data are represented as mean ± SD.

(B) Semiquantification of TREM2 levels using immunoblot grayscale analysis in the aforementioned cohort of 41 independent paired human GBM samples. Two-tailed paired t test.

(C) Left, representative IF images (with H&E staining) showing the infiltrated myeloid cells ($IBA1^{+}$) and their TREM2 expression levels in paired peritumoral and tumoral human GBM tissues. Scale bar, 500 μm (H&E and IF overview), 20 μm (magnified views in the middle), or 10 μm (rightmost magnified merged view). Right, quantification of $IBA1^{+}$ cell proportion and the mean fluorescence intensity (MFI) of TREM2 on these cells in randomly selected microscopy fields of each IF image. The thick dashed centerlines indicate the median. The thin dashed lines flanking the centerlines indicate the first and third quartiles. The whiskers indicate the maxima and minima. n = 51 independent GBM samples. Two-tailed paired t test.

(D) Illustration of scRNA-seq and spatial transcriptomics profiling of human glioma samples.

(E) UMAP plot of the identified cell clusters in the human glioma samples.

(F) Measured *TREM2* levels are shown by a color gradient as indicated in the UMAP plot of peritumoral and tumoral samples, respectively. *TREM2* levels are color coded, ranging from gray (low expression levels) to cyan (high expression levels).

(G–I) Violin-box plots showing *TREM2* levels between peritumoral and tumoral samples in the whole myeloid subset (G), in three paired samples (H), or in MG and infiltrated MDMs (I).

(J) HE-stained sections of the human high-grade glioma samples HT34 (left) and HT40 (right). The section regions on the slide are separated into four clusters, namely, the normal, peritumor, tumor, and tumor core. The *AIF1* (IBA1)-expressing and *TREM2*-expressing (with color gradients) points are shown on the sections. Scale bar, 1 mm. *TREM2* levels are color coded, ranging from bright red (low expression levels) to dark red (high expression levels).

(K and L) Left, color gradient plot showing TREM2 expression across tissue sections from HT34 (K) and HT40 (L). The black arrow indicates the direction from the peritumoral tissue to the tumor core. Middle, Line plot showing the inferred TREM2 expression along the trajectory. Right, Violin-box plots showing TREM2 expression in each indicated cluster. Games-Howell post hoc test. Scale bar, 1 mm. *TREM2* levels are color coded, ranging from bright red (low expression levels) to dark red (high expression levels).

(M) Survival analysis of three GBM cohorts based on public bulk RNA-seq data obtained from OncoInc (TCGA, RNASeqV2), PrognoScan (GSE7696), and the CGGA (mRNAseq693) database. Log rank test. ns, nonsignificant.

(N) Survival analysis investigating the involvement of TREM2-NEG in the OS (left) or the PFI (right) in the GBM TCGA-CDR dataset. Log rank test.

(O) Survival analysis of the in-house GBM cohort in (C). The cases were stratified by the median of TREM2 MFI (n = 51 independent samples). Log rank test.

For the violin-box plots in (G–I), (K), and (L), the centerlines indicate the median. The box limits indicate the first and third quartiles. The whiskers indicate the maxima and minima.

See also Figure S5 and Table S3.

Please cite this article in press as: Zhong et al., Distinct roles of TREM2 in central nervous system cancers and peripheral cancers, Cancer Cell (2024), https://doi.org/10.1016/j.ccell.2024.05.001

in tumoral myeloid cells compared to their peritumoral counterparts. IF staining of IBA1 and TREM2 also showed a similar pattern as observed in the murine samples (Figure S5C); there were markedly increased myeloid cells (IBA1$^+$) in tumoral areas with attenuated TREM2 intensity in each single cell (Figure 4C). The markedly augmented infiltration of myeloid cells may explain the overall overexpression of TREM2 in the cancerous group indicated by the TCGA dataset (Figure S1E), which does not permit the quantification of TREM2 levels in each single cell in GBM tissue owing to bulk RNA-seq methods. Flow cytometry profiling of paired fresh GBM samples confirmed the decreased TREM2 levels on both MG and MDMs (Figure S5F).

To substantiate the findings of TREM2 alterations in the TME of human GBM, we performed scRNA-seq on human glioma cancerous (T, $n = 5$) and peritumoral (P, $n = 4$) tissues (containing three paired samples) (Figure 4D). 94,577 high-quality cells were detected and clustered into 16 subsets (Figures 4E and S5G). TREM2 expression was centered on the major myeloid subsets (Figure S5H). In the cancerous tissues, an obvious decrease in TREM2 expression levels was found in the myeloid subsets (Figures 4F and 4G) and this finding was observed in each paired sample (Figure 4H). The same patterns were also observed for MG and MDMs (Figure 4I). Compared to MG, more obvious TREM2 downregulation in the tumoral group was seen in MDMs.

To gain deeper insights into spatial organization information, we examined three human high-grade glioma slides (all containing areas spanning peritumoral and tumoral tissues) by spatial transcriptomics (ST, 10× Visium platform) (Figure 4D). For each slide, the areas were categorized into four distinct types: normal, peritumor, tumor, and tumor core regions (Figures 4J, S5I, and S5J), consistent with the hematoxylin and eosin (HE) staining results. TREM2 expression distribution was colocalized with the myeloid cell marker *AIF1* (IBA1) in these ST sections. Notably, spatial trajectory analysis highlighted high TREM2 expression in the peritumoral area and comparatively lower TREM2 expression in the tumor area, with the tumor core expressing the lowest levels (Figures 4K, 4L, and S5K), in line with the aforementioned results.

Survival analysis using multiple bulk RNA-seq GBM datasets from TCGA, Chinese Glioma Genome Atlas (CGGA), and PrognoScan failed to reveal any significant difference between the *TREM2*^{high} and *TREM2*^{low} groups based on the median cutoff (Figure 4M). In contrast, high expression of *TREM2*-negatively correlated genes (TREM2-NEG, consisting of the top 50 upregulated genes (p_val_adj <0.05 and ordered by avg_log2FC) in TREM2-deficient TAMG identified in the mouse scRNA-seq (GBM vs. GBM KO), Table S3), were found to correlate with inferior OS and progression-free interval (PFI) after analyzing a GBM cohort from the TCGA Clinical Data Resource (TCGA-CDR) datasets[51] (Figure 4N), supporting that TREM2 maintains a protective landscape in the GBM TME. In our IF-staining cohort, higher TREM2 MFI in myeloid cells was correlated with better OS in these GBM patients (Figure 4O).

TREM2 overexpression in myeloid cells represses GBM growth and synergizes with immune checkpoint blockade (ICB) therapy

Given that GBM progression downregulated TREM2 expression in myeloid cells, we next investigated whether elevating TREM2 expression in TAMs can effectively impede GBM development. To efficiently overexpress TREM2 in MG and MDMs, we utilized an adeno-associated virus vector (AAV9-F4/80-TREM2-flag) to deliver TREM2. The AAV was intracranially injected at day 3 and day 10 after tumor inoculation, targeting resident MG and later on infiltrated MDMs, respectively (Figure 5A). This AAV serotype has been confirmed to have tropism toward the brain and MG and can effectively express its transgene for over six months.[52–54] The incorporated F4/80 promoter sequence also ensures selective TREM2 overexpression in MG and MDMs.[55] The selective TREM2 overexpression on myeloid subsets was validated by TREM2 immunoblotting on sorted CD11b$^+$ cells (Figure S6A) and flow cytometry (Figure S6B). Elevating TREM2 expression resulted in repressed GBM growth and prolonged OS in both GL261 and CT-2A GBM models (Figures 5B and 5C). Similar results for inhibited tumor growth and prolonged OS were observed when GBM-bearing *Trem2*$^{-/-}$ mice were treated with AAV-mediated TREM2 re-expression (Figures S6C and S6D), indicating that maintaining TREM2 levels is important for suppressing GBM progression.

To investigate how TREM2 overexpression changes the immune landscape of GBM, we applied scRNA-seq to profile the TME of the GL261 model treated with vector or AAV-TREM2. 66,643 cells were obtained and subjected to UMAP clustering (Figure 5D). Selective TREM2 overexpression was observed in the MG and MDM subsets (Figure 5E). AAV administration redirected the myeloid components toward immune-active phenotypes, as evidenced by upregulated proinflammatory signatures (*Il1b*, *Il1a*, *Tnf*, *Cd86*, and *Cd80*) and downregulated anti-inflammatory signatures (*Mrc1*, *Arg1*, *Chil3*, *Cd163*, and *Tgfbi*) in the MG and MDMs (Figure S6F). Upon AAV-TREM2 administration, T cells exhibited improved activity (Figure S6F), marked by downregulated naive signatures (*Lef1*, *Sell*, and *Tcf7*) but upregulated signatures related to activation or effector function (*Icos*, *Cd69*, *Cd28*, *Ifng*, *Prf1*, and *Gzmb*). Pathway analysis indicated that AAV-TREM2 administration upregulated inflammatory immune responses in the MG and MDM subsets, and the upregulated terms were associated with enhanced antitumor function in T cells (Figure 5F). These results were in concert with the flow cytometry validation using canonical markers (Figures 5G and 5H).

Since the AAV specifically targeted the myeloid cell compartment and pronounced CTL exhaustion was observed in the GBM TME (Figure 3C), we asked whether this treatment can be combined with the T cell-targeting ICB therapy. We treated the mice with AAV-TREM2 and intraperitoneal injection of anti-PD-1 antibody (10 mg/kg, every 5 days) (Figure 5I). Compared to AAV-TREM2 monotherapy, the combination therapy further impeded tumor proliferation and extended OS (Figures 5J and 5K), exhibiting strong synergistic effects.

CNS microenvironment defines the distinct role of TREM2 in GBM

We next sought to investigate the mechanisms underlying the distinct function of TREM2 in GBM. To define whether GBM-intrinsic features are involved, we intracranially injected a breast cancer cell line, EO771,[56] into wild-type and *Trem2*$^{-/-}$ mice. Similar to GBM tumors, EO771 tumors displayed accelerated growth and worse survival in *Trem2*$^{-/-}$ mice (Figures 6A–6C).

Please cite this article in press as: Zhong et al., Distinct roles of TREM2 in central nervous system cancers and peripheral cancers, Cancer Cell (2024), https://doi.org/10.1016/j.ccell.2024.05.001

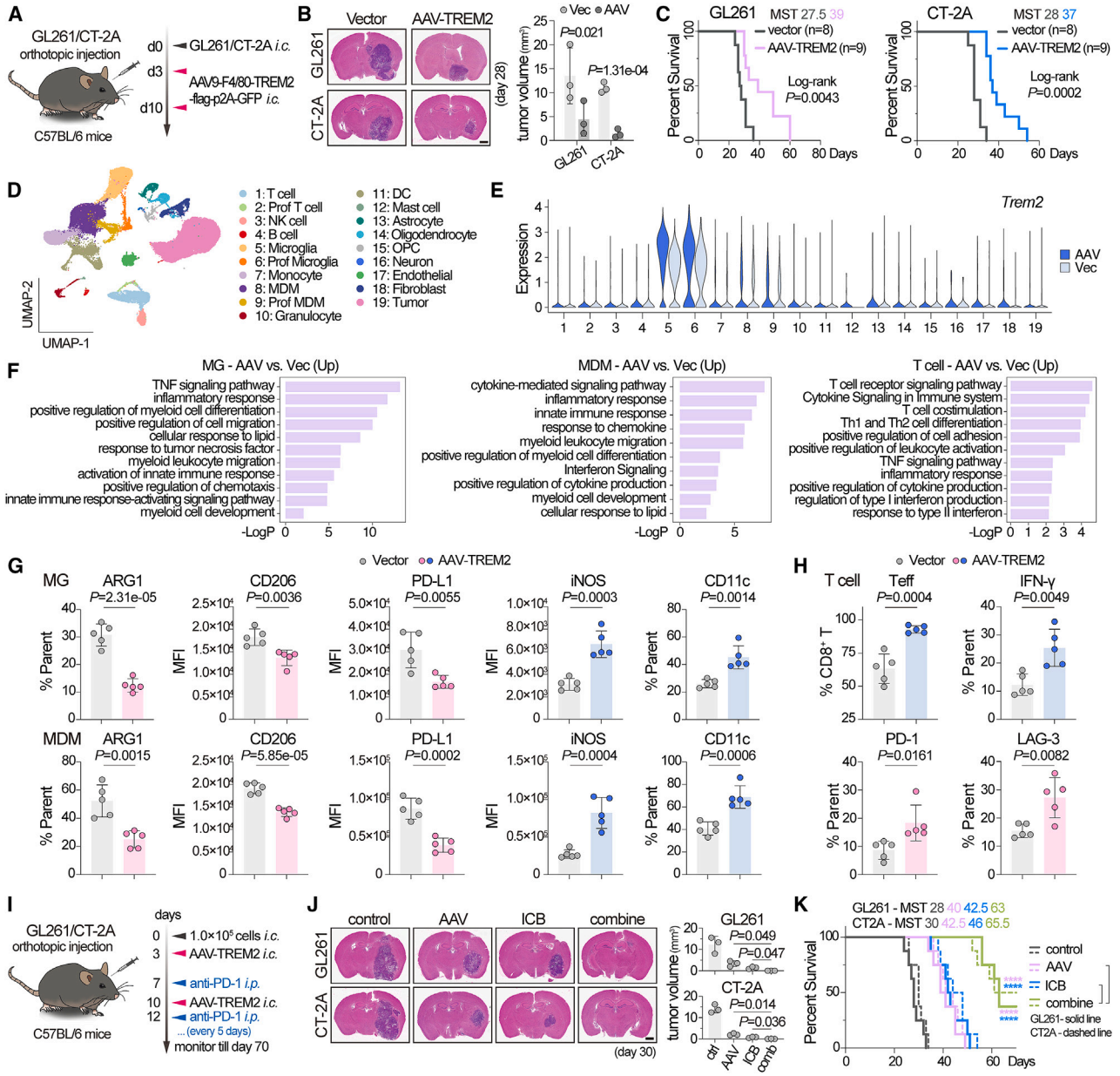

Figure 5. TREM2 overexpression in myeloid cells represses GBM growth and synergizes with ICB therapy

(A) Illustration of AAV treatment in GBM model mice.

(B) Representative and quantification (n = 3) of HE-stained brain sections from control vector or AAV-TREM2 treated GBM-bearing mice. Scale bar, 1 mm. Two-tailed paired t test.

(C) Kaplan-Meier analysis of the control vector (n = 8) or AAV-TREM2 (n = 9) treated GBM-bearing mice. Log rank test.

(D) UMAP plot of identified cell clusters in the TME of control vector- or the AAV-TREM2 treated GL261-GBM-bearing mice. n = 3 per group.

(E) Violin plot showing TREM2 expression in each identified cell cluster.

(F) Pathway analysis showing enriched upregulated terms in MG, MDM and T cell clusters of the AAV-TREM2 group.

(G) Phenotype profiling of infiltrated MG and MDMs by flow cytometry examination of conventional M2-like (ARG1, CD206, and PD-L1) and M1-like (iNOS and CD11c) markers. n = 5 per group. Two-tailed unpaired t test.

(H) Flow cytometry analysis of the proportion, effector status (IFN-γ) and exhaustion status (PD-1 and LAG-3) of effector $CD8^+$ T cells. n = 5 per group. Two-tailed unpaired t test.

(I) Illustration of AAV treatment, anti-PD-1 (ICB) treatment or combined treatment at the indicated timepoints.

(J) Representative and quantification (n = 3) of HE-stained brain sections from the indicated groups. Scale bar, 1 mm. Two-tailed paired t test.

(K) Kaplan-Meier analysis of the indicated groups. n = 8 per group. MST, median survival time. Solid lines, GL261 model. Dashed lines, CT2A model. Log rank test. ****$p < 0.0001$.

Data are represented as the mean ± SD in (B), (G), (H), and (J).

See also Figure S6.

Please cite this article in press as: Zhong et al., Distinct roles of TREM2 in central nervous system cancers and peripheral cancers, Cancer Cell (2024), https://doi.org/10.1016/j.ccell.2024.05.001

CellPress

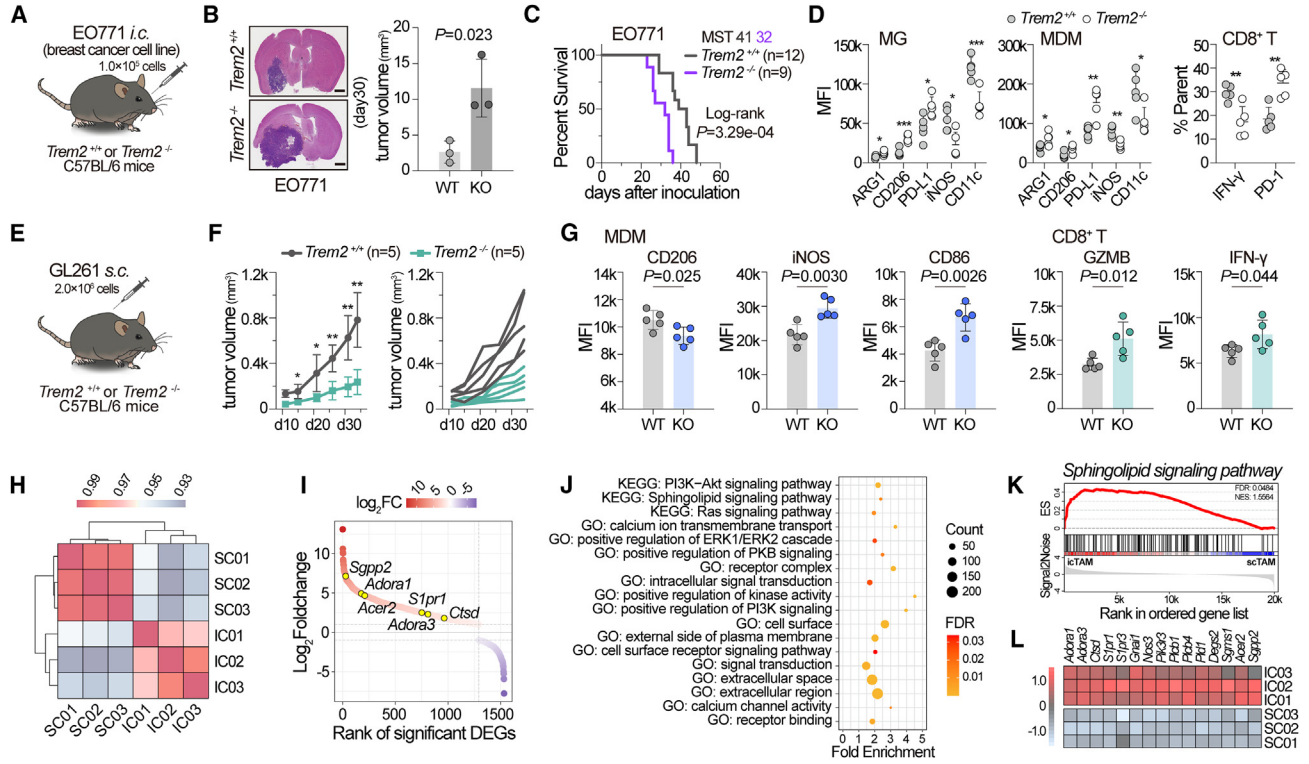

Figure 6. CNS microenvironment defines the distinct role of TREM2 in GBM

(A) Illustration of the brain EO771 model established in *Trem2*$^{+/+}$ and *Trem2*$^{-/-}$ mice. *i.c.*, intracranial injection.

(B and C) Representative and quantification of HE-stained brain sections (B) and survival analysis (C) of the EO771-tumor-bearing *Trem2*$^{+/+}$ (n = 12) and *Trem2*$^{-/-}$ (n = 9) mice. Scale bar, 1 mm. Two-tailed paired t test in (B). Log rank test in (C).

(D) Flow cytometry profiling of MG (left), infiltrated MDMs (middle) and CD8$^+$ T cells (right) in the TME of the brain EO771 model. n = 5 per group. Two-tailed unpaired t test. $^*p < 0.05$, $^{**}p < 0.01$, $^{***}p < 0.001$.

(E) Illustration of the subcutaneous GL261 model established in *Trem2*$^{+/+}$ and *Trem2*$^{-/-}$ mice. *s.c.*, subcutaneous injection.

(F) Growth curves of subcutaneous GL261 tumor in *Trem2*$^{+/+}$ and *Trem2*$^{-/-}$ mice. Tumor growth in each individual mouse is shown on the right. n = 5 per group. Two-tailed unpaired t test at each time point. $^*p < 0.05$, $^{**}p < 0.01$.

(G) Flow cytometry profiling of infiltrated MDMs and CD8$^+$ T cells in the TME of the subcutaneous GL261 model mice. n = 5 per group. Two-tailed unpaired t test.

(H) Heatmap drawn by gene expression pearson analysis showing clear distinction between the transcriptomes of icTAMs (IC) and scTAMs (SC). Correlation levels are color coded, ranging from blue (low levels) to red (high levels).

(I) Waterfall plot showing the significant DEGs between icTAMs and scTAMs.

(J) Bubble plot showing GO and KEGG pathway enrichment analysis of the significantly upregulated DEGs in icTAMs.

(K) GSEA showing that the sphingolipid signaling pathway is enriched in icTAMs.

(L) Heatmap comparing the expression of genes related to the sphingolipid signaling pathway between icTAMs (IC) and scTAMs (SC). Gene expression levels are color coded, ranging from blue (low expression levels) to red (high expression levels).

Data are represented as the mean ± SD in (B), (D), (F), and (G).

See also Figure S7 and Table S4.

Flow cytometry revealed a more immune-hostile TME in these mice, marked by enlarged population of M2-like immunosuppressive TAMs and exhausted CD8$^+$ T cells and decreased number of effector T cells (Figure 6D). These results suggest that tumor-intrinsic characteristics are unlikely to determine the function of TREM2 during CNS carcinogenesis.

In contrast, when GL261 cells were subcutaneously implanted, TREM2 deficiency resulted in arrested proliferation of inoculated tumor cells (Figure 6E and 6F) and a transition of the TME toward a proinflammatory and effectively antitumor state, as marked by downregulated CD206 but upregulated M1-like markers (iNOS and CD86) in MDMs and effector markers (IFN-γ and GZMB) in CD8$^+$ T cells (Figure 6G), similar to recently reported results using other non-CNS tumor cell lines.[8] These findings indicate that tumor-extrinsic or microenvironmental factors rather than tumor-intrinsic factors mediate the opposing roles of TREM2 in CNS and peripheral cancers.

To probe the potential cause, we sorted CD11b$^+$ myeloid cells (representing TREM2-expressing cells[1]) from GL261 intracranial and subcutaneous tumors (icTAMs and scTAMs) and performed bulk RNA-seq to investigate TREM2-related responses in these cells. The transcriptomes of icTAM were clearly distinguished from those of scTAM (Figure 6H). A list of 1,532 significantly differentially expressed genes (DEGs) was obtained (Figure 6I; Table S4). The upregulated DEGs were enriched in gene ontology (GO) terms related to membrane components and signaling transduction, including external side of the plasma membrane, cell surface receptor signaling pathway, and

Please cite this article in press as: Zhong et al., Distinct roles of TREM2 in central nervous system cancers and peripheral cancers, Cancer Cell (2024), https://doi.org/10.1016/j.ccell.2024.05.001

intracellular signal transduction (Figure 6J; Table S4). Pathway terms downstream of TREM2-DAP10/12, such as calcium ion transmembrane transport and the PI3K-AKT pathway,[1,11] were also enriched (Figure 6J; Table S4). These results indicated that the major differences between icTAMs and scTAMs were exhibited at the signal sensing surface and subsequent signaling transduction pathways, suggesting different stimulation by ligands derived from the microenvironment.

Further gene set enrichment analysis (GSEA) and gene set variation analysis (GSVA) both supported that icTAMs were more associated with the sphingolipid-related pathways (Figures 6K, S7A, and S7B; Table S4). Significant upregulation of several genes (*Sgpp2*, *Adora1*, and *Acer2*) related to the sphingolipid signaling pathway was identified in icTAMs (Figures 6I and 6L). Sphingolipids are one kind of TREM2 ligands that are highly enriched in the CNS microenvironment during pathological conditions, including cancer.[3,4,57] We next sought to identify the specific ligands responsible for the characteristic function of TREM2 in CNS cancers.

Sphingolipid-TREM2-signaling reprograms TAMs into an antitumor state

TREM2 serves as a membrane-bound sensor of environmental change and mediates multifaceted downstream signaling upon binding with different ligands (a wide panel of metabolites, including phospholipids and anionic carbohydrates).[2] We speculated that unspecified lipid ligands of TREM2 enriched in the CNS TME may result in the distinct TREM2-related antitumor response. To define the potential lipid ligand, we analyzed metabolomics data profiling the cerebrospinal fluid (CSF) collected from 21 GBM and 4 control patients (Figure 7A). A total of 656 lipidic metabolites were identified (Figure 7B; Table S5). Notably, sphingolipid metabolism stood out from the pathway enrichment analysis of the upregulated metabolites (Figure 7C; Table S5), in concert with the findings of bulk RNA-seq analysis.

The abundance of sphingomyelins (SM) and glycosphingolipids (GSL), both involved in sphingolipid metabolism, was markedly increased in the CSF of GBM (Figure 7B). They are common lipids in the CNS TME during tumor progression, releasing from tumor-disrupted myelin sheaths and other neuronal structures that are highly enriched in the CNS but much less distributed in peripheral pathological conditions.[57–61] We chose the representative forms of these lipids and subjected them to docking analysis to simulate their binding with TREM2. Both SM and GSL (ganglioside GM1) fit well with the basic patch on the TREM2 extracellular domain[2] (Figure 7D). A reporter cell assay supported the binding of these two lipids to TREM2 (Figure S7C). TREM2 can activate SYK-PI3K-AKT signaling upon sensing various kinds of lipids.[3,62] We next determined whether these CNS-enriched SM/GSLs were responsible for eliciting protective signaling in a TREM2-dependent fashion in GBM TAMs.

To this end, we sorted TAMs from the GL261 GBM and incubated them with purified SM and GM1. Treatment with gradient concentrations of SM and GM1 defined the optimal concentrations as 0.2 μg/mL and 0.5 μM, respectively (Figure 7E). SM/GM1 stimulation dramatically downregulated the M2-like markers CD206 and ARG1 while upregulating the M1-like markers iNOS and MHC-II[63] (Figure 7F). The levels of phospho-STAT3, a key regulator in M2 polarization, decreased upon SM/GM1 treatment, while the levels of M1-related phospho-STAT1 increased[64] (Figure 7F).

The involvement of SYK and AKT signaling in macrophage polarization has been extensively studied.[65–68] Of the three AKT isoforms, AKT2 is particularly associated with M1-like polarization.[68] Notably, phospho-SYK and downstream phospho-AKT2 were upregulated upon SM/GM1 stimulation (Figure 7G), while the anti-inflammatory-related isoform AKT1 remained unaltered (Figure S7D). The aforementioned effects were absent in TAMs sorted from *Trem2*$^{-/-}$ mice (Figures 7F and 7G), suggesting that reprogramming by SM/GM1 was TREM2-dependent.

In TAMs isolated from human GBM, SM/GM1 stimulation also resulted in a transition from an M2-like phenotype to an M1-like phenotype (Figures 7H and 7I). As assessed by qPCR, a wider panel of M2-like signature genes (*Cd163*, *Arg1*, *Mrc1*, *Stab1*, *Il10*, *F13a1*, and *Chil3*) were markedly downregulated upon SM/GM1 stimulation, accompanied by upregulated M1-like signatures (*Il12a*, *Il1a*, *Cd86*, and *Nos2*) (Figure 7J). SM/GM1-stimulated TAMs became less inhibitory of T cell proliferation (Figure 7K). The phagocytic activity of SM/GM1-stimulated TAMs was significantly increased (Figure 7L). Additionally, in the myelin sheath disruption-enriched area of the CNS cancer models, the proinflammatory marker CD11c[63] was upregulated in the infiltrated myeloid cells (Figures S7E and S7F). In spatial sequenced human GBM slides, a correlation between myelin sheath disruption and inflammatory response was observed (Figure S7G).

Overall, these results altogether indicate that CNS-enriched sphingolipids are capable of directing TAMs via TREM2 toward a defender state against GBM.

DISCUSSION

Increasing evidence underlines the immunosuppressive role of TREM2 in various malignancies where TREM2 defines an immunosuppressive macrophage subset or activates senescent-like tumor-promotive programs after sensing cancer-derived factors.[8,37,69] TREM2 has been comprehensively studied in neurodegenerative diseases, with crucial functions in recognizing damage-induced factors and potentiating metabolic fitness and neuroprotective processes.[62,70] It is conceivable that the role of TREM2 can be redirected to maintain CNS homeostasis during tumorigenesis. Previously, TREM2 was suggested as a therapeutic target for GBM based on bulk RNA-seq analysis and loss-of-function studies using TREM2 knockdown GBM cell lines.[71] However, the bulk RNA-seq failed to pinpoint the TREM2-expressing cells. Our in-house and published scRNA-seq data reveal that TREM2 is specifically expressed in myeloid subsets rather than cancer cells.[1] Most recently, TREM2 inhibition was reported to trigger antitumor activity in GBM.[72] However, the TREM2-deficient mouse strain and the GBM cell lines were different from the ones used here. Furthermore, this study treated the mice with a brain-penetrant CSF-1R inhibitor after tumor implantation, which is known to disrupt the TAMs.

Here, we observe that TREM2 plays a distinct immunoprotective role in the context of CNS malignancies. Unlike peripheral cancers, loss of TREM2 at the single-cell level in the TME may be a critical event during GBM progression. Experimental disruption of TREM2 robustly simulated this process and thus resulted in inferior survival outcomes. TREM2 loss may result from

Please cite this article in press as: Zhong et al., Distinct roles of TREM2 in central nervous system cancers and peripheral cancers, Cancer Cell (2024), https://doi.org/10.1016/j.ccell.2024.05.001

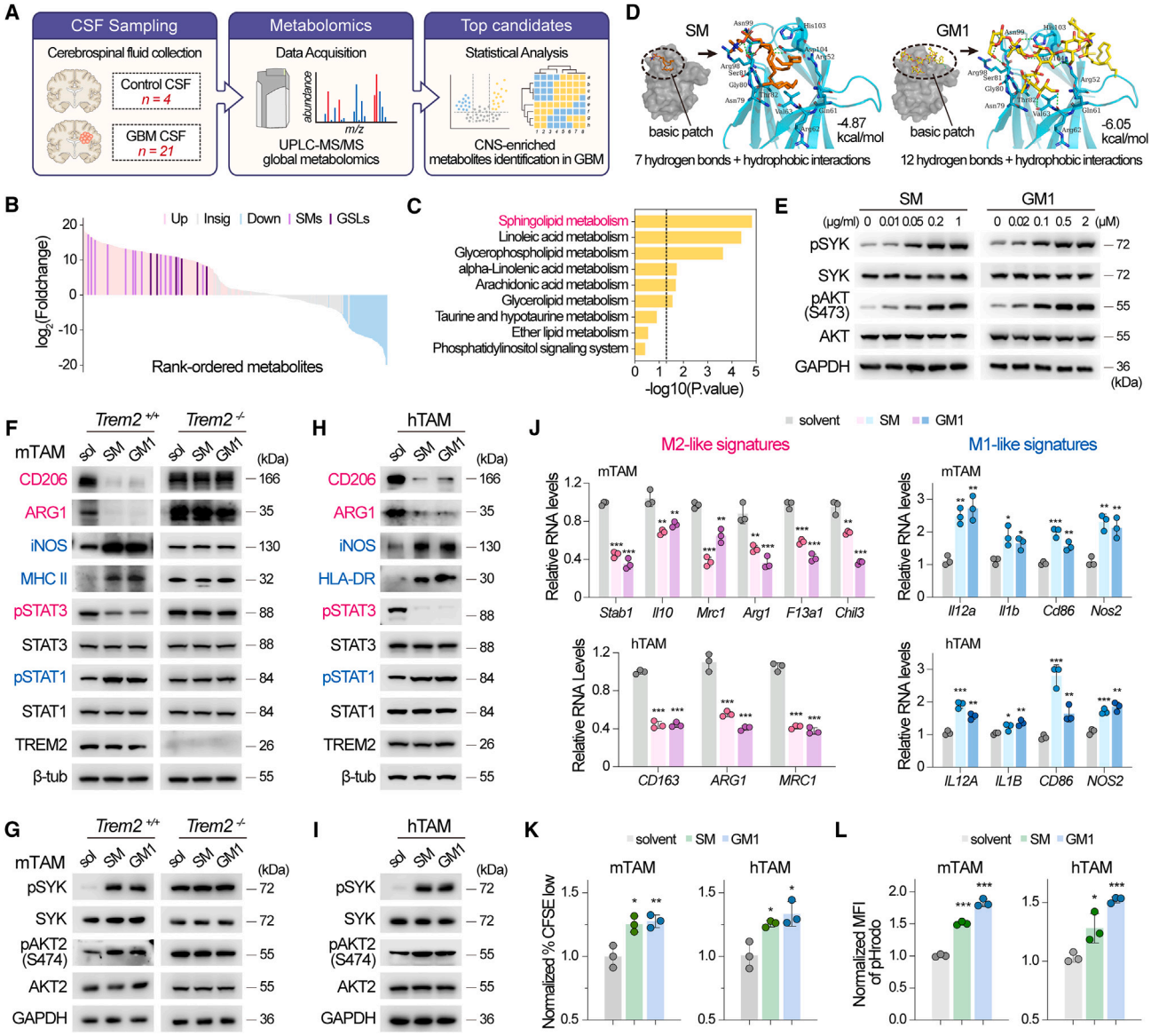

Figure 7. Sphingolipid-TREM2-signaling reprograms TAMs into an antitumor state

(A) Workflow illustration of CSF metabolomics profiling.

(B) Waterfall plot showing the differentially altered lipidic metabolites (GBM vs. control). Insig, insignificant. A metabolite with $p < 0.05$ and VIP (variable importance in projection) ≥ 1 was considered significantly altered.

(C) KEGG pathway enrichment analysis showing the significance of lipidic metabolic pathways. Hypergeometric test. The dash line indicates $p = 0.05$.

(D) Molecular docking analysis shows the key interactions between TREM2 and SM (orange) or between TREM2 and GM1 (yellow). TREM2 is shown in gray, or in cyan for the magnified view.

(E) Immunoblotting of phospho-SYK and downstream phospho-AKT levels in primary TAMs isolated from GL261 GBM model mice after SM/GM1 stimulation at the indicated concentrations. Representative of three independent experiments.

(F–I) (F and H) Immunoblotting of conventional M2-like markers (CD206, ARG1, and phospho-STAT3), M1-like markers (iNOS, HLA-DR, and phospho-STAT1), and TREM2 in SM (0.2 μg/mL for 48 h) or GM1 (0.5 μM for 48 h) stimulated primary TAMs from model mice (F, mTAM) or human GBM samples (H, hTAM). (G and I) Immunoblotting of phospho-SYK and phospho-AKT2 levels in the aforementioned SM/GM1-or solvent-stimulated primary mTAM (G) and hTAM (I). Representative of three independent experiments.

(J) Relative mRNA levels of M1-like and M2-like gene signatures in the aforementioned SM/GM1-stimulated mTAM and hTAM. n= 3 independent experiments. Two-tailed unpaired t test. $^{*}p < 0.5$, $^{**}p < 0.01$, $^{***}p < 0.001$.

(K) Proliferation assay of $CD3^{+}$ T cells cocultured with SM/GM1 or solvent stimulated mTAM and hTAM. $n = 3$ independent experiments. Two-tailed unpaired t test. $^{*}p < 0.5$, $^{**}p < 0.01$, $^{***}p < 0.001$.

(L) Phagocytosis assay of SM/GM1 or solvent stimulated mTAM and hTAM. $n = 3$ independent experiments. MFI, median fluorescence intensity. Two-tailed unpaired t test. $^{*}p < 0.5$, $^{***}p < 0.001$.

Data are represented as the mean ± SD in (J–L).

See also Figure S7 and Table S5.

microenvironmental factors predominantly existing within the GBM TME, such as the myelin debris released during tumor expansion or IL-10 and other secretive factors.[73,74] The upstream mechanisms of TREM2 loss in the GBM TAMs remain a critical area for further investigations.

We determined that SM/GSL, markedly upregulated lipids in the CNS TME during tumor expansion that destroys CNS-specific structures such as myelin sheaths and neurons, are responsible for activating TREM2 protective signaling. Due to the lack of such structures, these ligands are absent in the TME of peripheral cancers, which explains the disparate response patterns downstream of TREM2. A recent study has signified the critical involvement of SYK signaling (downstream of TREM2) in coordinating protective microglial activation upon binding damaged myelin during neurodegenerative diseases.[75] However, the underlying mechanism of CNS-enriched damage-induced lipids reprograming TREM2-expressing cells is lacking. In our study, we discovered predominant activation of AKT2 in GBM TAMs upon SM/GSL stimulation, consequently leading to preferential M1-like polarization and enhanced antitumor responses of myeloid cells. However, whether additional factors exist merits further investigation.

Based on the observations of TREM2 loss and its antitumor role in GBM, we restored TREM2 expression and observed a pronounced antitumor efficacy. A more apparent decrease in TREM2 levels in MDMs than in MG was observed during GBM progression. Since MDMs are more closely associated with GBM patient survival than MG, recovering the innate antitumor function of MDMs may result in more benefits for GBM patients.[14,22] Our results suggest that TREM2 is an organ-specific TAM target that requires different strategies depending on the microenvironmental cues. For cancers that are characterized by TREM2 receptor downregulation but are enriched with protective signaling ligands, TREM2 overexpression represents a promising therapy.

In summary, our study uncovers the distinct function of TREM2 in CNS cancers and the underlying mechanistic clues and reveals that restoring rather than suppressing TREM2 expression may represent a disease-specific treatment approach for GBM.

STAR★METHODS

Detailed methods are provided in the online version of this paper and include the following:

SUPPLEMENTAL INFORMATION

Supplemental information can be found online at https://doi.org/10.1016/j.ccell.2024.05.001.

ACKNOWLEDGMENTS

We sincerely appreciate all the patients who participated in the study. This work was supported by the National Science Fund for Distinguished Young Scholars (82125024 and T2125002), the National Natural Science Foundation of China (82192890, 82192894, 823B2063, 82341007, 82241230, 82373191, and 82072779), Guangdong Province Regional Joint Fund (2022B1515120023), the New Cornerstone Science Foundation through the XPLORER PRIZE, the Postdoctoral Fellowship of Bo Ya and Beijing Natural Science Foundation (Z220014).

AUTHOR CONTRIBUTIONS

Experiment design: N. Z., F. B., and J. Z.; investigation and data curation: J. Z., Y. G., H. S., Y. L., and K. D.; bioinformatic analysis: X. X., L. P., C. L., and J. Z.; writing: J. Z., X. X., F. B., and N. Z.; scientific input and editing: X. W., Y. S., F. X., and Y.Y.

DECLARATION OF INTERESTS

The authors declare no competing interests.

Received: October 2, 2023
Revised: February 26, 2024
Accepted: May 1, 2024
Published: May 23, 2024

REFERENCES

1. Deczkowska, A., Weiner, A., and Amit, I. (2020). The Physiology, Pathology, and Potential Therapeutic Applications of the TREM2 Signaling Pathway. Cell *181*, 1207–1217. https://doi.org/10.1016/j.cell.2020.05.003.
2. Kober, D.L., and Brett, T.J. (2017). TREM2-Ligand Interactions in Health and Disease. J. Mol. Biol. *429*, 1607–1629. https://doi.org/10.1016/j.jmb.2017.04.004.
3. Wang, Y., Cella, M., Mallinson, K., Ulrich, J.D., Young, K.L., Robinette, M.L., Gilfillan, S., Krishnan, G.M., Sudhakar, S., Zinselmeyer, B.H., et al. (2015). TREM2 Lipid Sensing Sustains the Microglial Response in an Alzheimer's Disease Model. Cell *160*, 1061–1071. https://doi.org/10.1016/j.cell.2015.01.049.
4. Poliani, P.L., Wang, Y., Fontana, E., Robinette, M.L., Yamanishi, Y., Gilfillan, S., and Colonna, M. (2015). TREM2 sustains microglial expansion during aging and response to demyelination. J. Clin. Invest. *125*, 2161–2170. https://doi.org/10.1172/JCI77983.
5. Xie, M., Liu, Y.U., Zhao, S., Zhang, L., Bosco, D.B., Pang, Y.-P., Zhong, J., Sheth, U., Martens, Y.A., Zhao, N., et al. (2022). TREM2 interacts with TDP-43 and mediates microglial neuroprotection against TDP-43-related neurodegeneration. Nat. Neurosci. *25*, 26–38. https://doi.org/10.1038/s41593-021-00975-6.

6. Atagi, Y., Liu, C.-C., Painter, M.M., Chen, X.-F., Verbeeck, C., Zheng, H., Li, X., Rademakers, R., Kang, S.S., Xu, H., et al. (2015). Apolipoprotein E Is a Ligand for Triggering Receptor Expressed on Myeloid Cells 2 (TREM2). J. Biol. Chem. *290*, 26043–26050. https://doi.org/10.1074/jbc.M115.679043.

7. Wolf, E.M., Fingleton, B., and Hasty, A.H. (2022). The therapeutic potential of TREM2 in cancer. Front. Oncol. *12*, 984193. https://doi.org/10.3389/fonc.2022.984193.

8. Molgora, M., Esaulova, E., Vermi, W., Hou, J., Chen, Y., Luo, J., Brioschi, S., Bugatti, M., Omodei, A.S., Ricci, B., et al. (2020). TREM2 Modulation Remodels the Tumor Myeloid Landscape Enhancing Anti-PD-1 Immunotherapy. Cell *182*, 886–900.e17. https://doi.org/10.1016/j.cell.2020.07.013.

9. Esparza-Baquer, A., Labiano, I., Sharif, O., Agirre-Lizaso, A., Oakley, F., Rodrigues, P.M., Zhuravleva, E., O'Rourke, C.J., Hijona, E., Jimenez-Agüero, R., et al. (2021). TREM-2 defends the liver against hepatocellular carcinoma through multifactorial protective mechanisms. Gut *70*, 1345–1361. https://doi.org/10.1136/gutjnl-2019-319227.

10. Tan, J., Fan, W., Liu, T., Zhu, B., Liu, Y., Wang, S., Wu, J., Liu, J., Zou, F., Wei, J., et al. (2023). TREM2+ macrophages suppress CD8+ T-cell infiltration after transarterial chemoembolisation in hepatocellular carcinoma. J. Hepatol. *79*, 126–140. https://doi.org/10.1016/j.jhep.2023.02.032.

11. Turnbull, I.R., and Colonna, M. (2007). Activating and inhibitory functions of DAP12. Nat. Rev. Immunol. *7*, 155–161. https://doi.org/10.1038/nri2014.

12. Hambardzumyan, D., Gutmann, D.H., and Kettenmann, H. (2016). The role of microglia and macrophages in glioma maintenance and progression. Nat. Neurosci. *19*, 20–27. https://doi.org/10.1038/nn.4185.

13. Andersen, B.M., Faust Akl, C., Wheeler, M.A., Chiocca, E.A., Reardon, D.A., and Quintana, F.J. (2021). Glial and myeloid heterogeneity in the brain tumour microenvironment. Nat. Rev. Cancer *21*, 786–802. https://doi.org/10.1038/s41568-021-00397-3.

14. Keane, L., Cheray, M., Blomgren, K., and Joseph, B. (2021). Multifaceted microglia — key players in primary brain tumour heterogeneity. Nat. Rev. Neurol. *17*, 243–259. https://doi.org/10.1038/s41582-021-00463-2.

15. Butowski, N., Colman, H., De Groot, J.F., Omuro, A.M., Nayak, L., Wen, P.Y., Cloughesy, T.F., Marimuthu, A., Haidar, S., Perry, A., et al. (2016). Orally administered colony stimulating factor 1 receptor inhibitor PLX3397 in recurrent glioblastoma: an Ivy Foundation Early Phase Clinical Trials Consortium phase II study. Neuro Oncol. *18*, 557–564. https://doi.org/10.1093/neuonc/nov245.

16. Klemm, F., Maas, R.R., Bowman, R.L., Kornete, M., Soukup, K., Nassiri, S., Brouland, J.-P., Iacobuzio-Donahue, C.A., Brennan, C., Tabar, V., et al. (2020). Interrogation of the Microenvironmental Landscape in Brain Tumors Reveals Disease-Specific Alterations of Immune Cells. Cell *181*, 1643–1660.e17. https://doi.org/10.1016/j.cell.2020.05.007.

17. Sampson, J.H., Gunn, M.D., Fecci, P.E., and Ashley, D.M. (2020). Brain immunology and immunotherapy in brain tumours. Nat. Rev. Cancer *20*, 12–25. https://doi.org/10.1038/s41568-019-0224-7.

18. Mathewson, N.D., Ashenberg, O., Tirosh, I., Gritsch, S., Perez, E.M., Marx, S., Jerby-Arnon, L., Chanoch-Myers, R., Hara, T., Richman, A.R., et al. (2021). Inhibitory CD161 receptor identified in glioma-infiltrating T cells by single-cell analysis. Cell *184*, 1281–1298.e26. https://doi.org/10.1016/j.cell.2021.01.022.

19. Yeo, A.T., Rawal, S., Delcuze, B., Christofides, A., Atayde, A., Strauss, L., Balaj, L., Rogers, V.A., Uhlmann, E.J., Varma, H., et al. (2022). Single-cell RNA sequencing reveals evolution of immune landscape during glioblastoma progression. Nat. Immunol. *23*, 971–984. https://doi.org/10.1038/s41590-022-01215-0.

20. Lim, M., Xia, Y., Bettegowda, C., and Weller, M. (2018). Current state of immunotherapy for glioblastoma. Nat. Rev. Clin. Oncol. *15*, 422–442. https://doi.org/10.1038/s41571-018-0003-5.

21. Jackson, C.M., Choi, J., and Lim, M. (2019). Mechanisms of immunotherapy resistance: lessons from glioblastoma. Nat. Immunol. *20*, 1100–1109. https://doi.org/10.1038/s41590-019-0433-y.

22. Friebel, E., Kapolou, K., Unger, S., Núñez, N.G., Utz, S., Rushing, E.J., Regli, L., Weller, M., Greter, M., Tugues, S., et al. (2020). Single-Cell Mapping of Human Brain Cancer Reveals Tumor-Specific Instruction of Tissue-Invading Leukocytes. Cell *181*, 1626–1642.e20. https://doi.org/10.1016/j.cell.2020.04.055.

23. Ochocka, N., Segit, P., Walentynowicz, K.A., Wojnicki, K., Cyranowski, S., Swatler, J., Mieczkowski, J., and Kaminska, B. (2021). Single-cell RNA sequencing reveals functional heterogeneity of glioma-associated brain macrophages. Nat. Commun. *12*, 1151. https://doi.org/10.1038/s41467-021-21407-w.

24. Pombo Antunes, A.R., Scheyltjens, I., Lodi, F., Messiaen, J., Antoranz, A., Duerinck, J., Kancheva, D., Martens, L., De Vlaminck, K., Van Hove, H., et al. (2021). Single-cell profiling of myeloid cells in glioblastoma across species and disease stage reveals macrophage competition and specialization. Nat. Neurosci. *24*, 595–610. https://doi.org/10.1038/s41593-020-00789-y.

25. Yin, W., Ping, Y.F., Li, F., Lv, S.Q., Zhang, X.N., Li, X.G., Guo, Y., Liu, Q., Li, T.R., Yang, L.Q., et al. (2022). A map of the spatial distribution and tumour-associated macrophage states in glioblastoma and grade 4 *IDH* -mutant astrocytoma. J. Pathol. *258*, 121–135. https://doi.org/10.1002/path.5984.

26. Yeini, E., Ofek, P., Pozzi, S., Albeck, N., Ben-Shushan, D., Tiram, G., Golan, S., Kleiner, R., Sheinin, R., Israeli Dangoor, S., et al. (2021). P-selectin axis plays a key role in microglia immunophenotype and glioblastoma progression. Nat. Commun. *12*, 1912. https://doi.org/10.1038/s41467-021-22186-0.

27. Wesolowska, A., Kwiatkowska, A., Slomnicki, L., Dembinski, M., Master, A., Sliwa, M., Franciszkiewicz, K., Chouaib, S., and Kaminska, B. (2008). Microglia-derived TGF-beta as an important regulator of glioblastoma invasion—an inhibition of TGF-beta-dependent effects by shRNA against human TGF-beta type II receptor. Oncogene *27*, 918–930. https://doi.org/10.1038/sj.onc.1210683.

28. Tseng, D., Vasquez-Medrano, D.A., and Brown, J.M. (2011). Targeting SDF-1/CXCR4 to inhibit tumour vasculature for treatment of glioblastomas. Br. J. Cancer *104*, 1805–1809. https://doi.org/10.1038/bjc.2011.169.

29. Pyonteck, S.M., Akkari, L., Schuhmacher, A.J., Bowman, R.L., Sevenich, L., Quail, D.F., Olson, O.C., Quick, M.L., Huse, J.T., Teijeiro, V., et al. (2013). CSF-1R inhibition alters macrophage polarization and blocks glioma progression. Nat. Med. *19*, 1264–1272. https://doi.org/10.1038/nm.3337.

30. Takenaka, M.C., Gabriely, G., Rothhammer, V., Mascanfroni, I.D., Wheeler, M.A., Chao, C.-C., Gutiérrez-Vázquez, C., Kenison, J., Tjon, E.C., Barroso, A., et al. (2019). Control of tumor-associated macrophages and T cells in glioblastoma via AHR and CD39. Nat. Neurosci. *22*, 729–740. https://doi.org/10.1038/s41593-019-0370-y.

31. Goswami, S., Walle, T., Cornish, A.E., Basu, S., Anandhan, S., Fernandez, I., Vence, L., Blando, J., Zhao, H., Yadav, S.S., et al. (2020). Immune profiling of human tumors identifies CD73 as a combinatorial target in glioblastoma. Nat. Med. *26*, 39–46. https://doi.org/10.1038/s41591-019-0694-x.

32. Hutter, G., Theruvath, J., Graef, C.M., Zhang, M., Schoen, M.K., Manz, E.M., Bennett, M.L., Olson, A., Azad, T.D., Sinha, R., et al. (2019). Microglia are effector cells of CD47-SIRPα antiphagocytic axis disruption against glioblastoma. Proc. Natl. Acad. Sci. USA *116*, 997–1006. https://doi.org/10.1073/pnas.1721434116.

33. Khan, F., Pang, L., Dunterman, M., Lesniak, M.S., Heimberger, A.B., and Chen, P. (2023). Macrophages and microglia in glioblastoma: heterogeneity, plasticity, and therapy. J. Clin. Invest. *133*, e163446. https://doi.org/10.1172/JCI163446.

34. Turnbull, I.R., Gilfillan, S., Cella, M., Aoshi, T., Miller, M., Piccio, L., Hernandez, M., and Colonna, M. (2006). Cutting Edge: TREM-2 Attenuates Macrophage Activation. J. Immunol. *177*, 3520–3524. https://doi.org/10.4049/jimmunol.177.6.3520.

35. Zhong, J., Wu, X., Gao, Y., Chen, J., Zhang, M., Zhou, H., Yang, J., Xiao, F., Yang, X., Huang, N., et al. (2023). Circular RNA encoded MET variant

promotes glioblastoma tumorigenesis. Nat. Commun. *14*, 4467. https://doi.org/10.1038/s41467-023-40212-1.

36. Sigalov, A.B. (2022). Inhibition of TREM-2 Markedly Suppresses Joint Inflammation and Damage in Experimental Arthritis. IJMS *23*, 8857. https://doi.org/10.3390/ijms23168857.

37. Bancaro, N., Calì, B., Troiani, M., Elia, A.R., Arzola, R.A., Attanasio, G., Lai, P., Crespo, M., Gurel, B., Pereira, R., et al. (2023). Apolipoprotein E induces pathogenic senescent-like myeloid cells in prostate cancer. Cancer Cell *41*, 602–619.e11. https://doi.org/10.1016/j.ccell.2023.02.004.

38. Park, M.D., Reyes-Torres, I., LeBerichel, J., Hamon, P., LaMarche, N.M., Hegde, S., Belabed, M., Troncoso, L., Grout, J.A., Magen, A., et al. (2023). TREM2 macrophages drive NK cell paucity and dysfunction in lung cancer. Nat. Immunol. *24*, 792–801. https://doi.org/10.1038/s41590-023-01475-4.

39. Kumar, V., Patel, S., Tcyganov, E., and Gabrilovich, D.I. (2016). The Nature of Myeloid-Derived Suppressor Cells in the Tumor Microenvironment. Trends Immunol. *37*, 208–220. https://doi.org/10.1016/j.it.2016.01.004.

40. Green, K.N., Crapser, J.D., and Hohsfield, L.A. (2020). To Kill a Microglia: A Case for CSF1R Inhibitors. Trends Immunol. *41*, 771–784. https://doi.org/10.1016/j.it.2020.07.001.

41. Kusmartsev, S., and Gabrilovich, D.I. (2006). Role Of Immature Myeloid Cells in Mechanisms of Immune Evasion In Cancer. Cancer Immunol. Immunother. *55*, 237–245. https://doi.org/10.1007/s00262-005-0048-z.

42. Kusmartsev, S., and Gabrilovich, D.I. (2003). Inhibition of myeloid cell differentiation in cancer: the role of reactive oxygen species. J. Leukoc. Biol. *74*, 186–196. https://doi.org/10.1189/jlb.0103010.

43. Corzo, C.A., Condamine, T., Lu, L., Cotter, M.J., Youn, J.-I., Cheng, P., Cho, H.-I., Celis, E., Quiceno, D.G., Padhya, T., et al. (2010). HIF-1α regulates function and differentiation of myeloid-derived suppressor cells in the tumor microenvironment. J. Exp. Med. *207*, 2439–2453. https://doi.org/10.1084/jem.20100587.

44. von Roemeling, C.A., Wang, Y., Qie, Y., Yuan, H., Zhao, H., Liu, X., Yang, Z., Yang, M., Deng, W., Bruno, K.A., et al. (2020). Therapeutic modulation of phagocytosis in glioblastoma can activate both innate and adaptive antitumour immunity. Nat. Commun. *11*, 1508. https://doi.org/10.1038/s41467-020-15129-8.

45. Bennett, M.L., Bennett, F.C., Liddelow, S.A., Ajami, B., Zamanian, J.L., Fernhoff, N.B., Mulinyawe, S.B., Bohlen, C.J., Adil, A., Tucker, A., et al. (2016). New tools for studying microglia in the mouse and human CNS. Proc. Natl. Acad. Sci. USA *113*, E1738–E1746. https://doi.org/10.1073/pnas.1525528113.

46. Kaiser, T., and Feng, G. (2019). Tmem119-EGFP and Tmem119-CreERT2 Transgenic Mice for Labeling and Manipulating Microglia. eNeuro *6*, ENEURO.0448-18.2019. https://doi.org/10.1523/ENEURO.0448-18.2019.

47. Vanneste, D., Bai, Q., Hasan, S., Peng, W., Pirottin, D., Schyns, J., Maréchal, P., Ruscitti, C., Meunier, M., Liu, Z., et al. (2023). MafB-restricted local monocyte proliferation precedes lung interstitial macrophage differentiation. Nat. Immunol. *24*, 827–840. https://doi.org/10.1038/s41590-023-01468-3.

48. Cook, R.S., Jacobsen, K.M., Wofford, A.M., DeRyckere, D., Stanford, J., Prieto, A.L., Redente, E., Sandahl, M., Hunter, D.M., Strunk, K.E., et al. (2013). MerTK inhibition in tumor leukocytes decreases tumor growth and metastasis. J. Clin. Invest. *123*, 3231–3242. https://doi.org/10.1172/JCI67655.

49. Ma, S.-R., Deng, W.-W., Liu, J.-F., Mao, L., Yu, G.-T., Bu, L.-L., Kulkarni, A.B., Zhang, W.-F., and Sun, Z.-J. (2017). Blockade of adenosine A2A receptor enhances CD8(+) T cells response and decreases regulatory T cells in head and neck squamous cell carcinoma. Mol. Cancer *16*, 99. https://doi.org/10.1186/s12943-017-0665-0.

50. Agresta, L., Hoebe, K.H.N., and Janssen, E.M. (2018). The Emerging Role of CD244 Signaling in Immune Cells of the Tumor Microenvironment. Front. Immunol. *9*, 2809. https://doi.org/10.3389/fimmu.2018.02809.

51. Liu, J., Lichtenberg, T., Hoadley, K.A., Poisson, L.M., Lazar, A.J., Cherniack, A.D., Kovatich, A.J., Benz, C.C., Levine, D.A., Lee, A.V., et al. (2018). An Integrated TCGA Pan-Cancer Clinical Data Resource to Drive High-Quality Survival Outcome Analytics. Cell *173*, 400–416.e11. https://doi.org/10.1016/j.cell.2018.02.052.

52. Berns, K.I., and Muzyczka, N. (2017). AAV: An Overview of Unanswered Questions. Hum. Gene Ther. *28*, 308–313. https://doi.org/10.1089/hum.2017.048.

53. Aschauer, D.F., Kreuz, S., and Rumpel, S. (2013). Analysis of transduction efficiency, tropism and axonal transport of AAV serotypes 1, 2, 5, 6, 8 and 9 in the mouse brain. PLoS One *8*, e76310. https://doi.org/10.1371/journal.pone.0076310.

54. Okada, Y., Hosoi, N., Matsuzaki, Y., Fukai, Y., Hiraga, A., Nakai, J., Nitta, K., Shinohara, Y., Konno, A., and Hirai, H. (2022). Development of microglia-targeting adeno-associated viral vectors as tools to study microglial behavior in vivo. Commun. Biol. *5*, 1224. https://doi.org/10.1038/s42003-022-04200-3.

55. Maes, M.E., Colombo, G., Schulz, R., and Siegert, S. (2019). Targeting microglia with lentivirus and AAV: Recent advances and remaining challenges. Neurosci. Lett. *707*, 134310. https://doi.org/10.1016/j.neulet.2019.134310.

56. Monteiro, C., Miarka, L., Perea-García, M., Priego, N., García-Gómez, P., Álvaro-Espinosa, L., de Pablos-Aragoneses, A., Yebra, N., Retana, D., Baena, P., et al. (2022). Stratification of radiosensitive brain metastases based on an actionable S100A9/RAGE resistance mechanism. Nat. Med. *28*, 752–765. https://doi.org/10.1038/s41591-022-01749-8.

57. Brooks, L.J., Clements, M.P., Burden, J.J., Kocher, D., Richards, L., Devesa, S.C., Zakka, L., Woodberry, M., Ellis, M., Jaunmuktane, Z., et al. (2021). The white matter is a pro-differentiative niche for glioblastoma. Nat. Commun. *12*, 2184. https://doi.org/10.1038/s41467-021-22225-w.

58. Yen, P.S., Teo, B.T., Chiu, C.H., Chen, S.C., Chiu, T.L., and Su, C.F. (2009). White matter tract involvement in brain tumors: a diffusion tensor imaging analysis. Surg. Neurol. *72*, 464–469. https://doi.org/10.1016/j.surneu.2009.05.008.

59. Olsen, A.S.B., and Færgeman, N.J. (2017). Sphingolipids: membrane microdomains in brain development, function and neurological diseases. Open Biol. *7*, 170069. https://doi.org/10.1098/rsob.170069.

60. Voets, N.L., Bartsch, A., and Plaha, P. (2017). Brain white matter fibre tracts: a review of functional neuro-oncological relevance. J. Neurol. Neurosurg. Psychiatry *88*, 1017–1025. https://doi.org/10.1136/jnnp-2017-316170.

61. Wang, J., Xu, S.-L., Duan, J.-J., Yi, L., Guo, Y.-F., Shi, Y., Li, L., Yang, Z.-Y., Liao, X.-M., Cai, J., et al. (2019). Invasion of white matter tracts by glioma stem cells is regulated by a NOTCH1–SOX2 positive-feedback loop. Nat. Neurosci. *22*, 91–105. https://doi.org/10.1038/s41593-018-0285-z.

62. Ulland, T.K., Song, W.M., Huang, S.C.-C., Ulrich, J.D., Sergushichev, A., Beatty, W.L., Loboda, A.A., Zhou, Y., Cairns, N.J., Kambal, A., et al. (2017). TREM2 Maintains Microglial Metabolic Fitness in Alzheimer's Disease. Cell *170*, 649–663.e13. https://doi.org/10.1016/j.cell.2017.07.023.

63. Zhai, K., Huang, Z., Huang, Q., Tao, W., Fang, X., Zhang, A., Li, X., Stark, G.R., Hamilton, T.A., and Bao, S. (2021). Pharmacological inhibition of BACE1 suppresses glioblastoma growth by stimulating macrophage phagocytosis of tumor cells. Nat. Can. (Ott.) *2*, 1136–1151. https://doi.org/10.1038/s43018-021-00267-9.

64. Sica, A., and Mantovani, A. (2012). Macrophage plasticity and polarization: in vivo veritas. J. Clin. Invest. *122*, 787–795. https://doi.org/10.1172/JCI59643.

65. Vergadi, E., Ieronymaki, E., Lyroni, K., Vaporidi, K., and Tsatsanis, C. (2017). Akt Signaling Pathway in Macrophage Activation and M1/M2 Polarization. J. Immunol. *198*, 1006–1014. https://doi.org/10.4049/jimmunol.1601515.

66. Liu, M., Luo, F., Ding, C., Albeituni, S., Hu, X., Ma, Y., Cai, Y., McNally, L., Sanders, M.A., Jain, D., et al. (2015). Dectin-1 Activation by a Natural Product β-Glucan Converts Immunosuppressive Macrophages into an M1-like Phenotype. J. Immunol. *195*, 5055–5065. https://doi.org/10.4049/jimmunol.1501158.

67. Xue, V.W., Chung, J.Y.-F., Tang, P.C.-T., Chan, A.S.-W., To, T.H.-W., Chung, J.S.-Y., Mussal, F., Lam, E.W.-F., Li, C., To, K.-F., et al. (2021). USMB-shMincle: a virus-free gene therapy for blocking M1/M2 polarization of tumor-associated macrophages. Mol. Ther. Oncolytics *23*, 26–37. https://doi.org/10.1016/j.omto.2021.08.010.

68. Arranz, A., Doxaki, C., Vergadi, E., Martinez De La Torre, Y., Vaporidi, K., Lagoudaki, E.D., Ieronymaki, E., Androulidaki, A., Venihaki, M., Margioris, A.N., et al. (2012). Akt1 and Akt2 protein kinases differentially contribute to macrophage polarization. Proc. Natl. Acad. Sci. USA *109*, 9517–9522. https://doi.org/10.1073/pnas.1119038109.

69. Katzenelenbogen, Y., Sheban, F., Yalin, A., Yofe, I., Svetlichnyy, D., Jaitin, D.A., Bornstein, C., Moshe, A., Keren-Shaul, H., Cohen, M., et al. (2020). Coupled scRNA-Seq and Intracellular Protein Activity Reveal an Immunosuppressive Role of TREM2 in Cancer. Cell *182*, 872–885.e19. https://doi.org/10.1016/j.cell.2020.06.032.

70. Keren-Shaul, H., Spinrad, A., Weiner, A., Matcovitch-Natan, O., Dvir-Szternfeld, R., Ulland, T.K., David, E., Baruch, K., Lara-Astaiso, D., Toth, B., et al. (2017). A Unique Microglia Type Associated with Restricting Development of Alzheimer's Disease. Cell *169*, 1276–1290.e17. https://doi.org/10.1016/j.cell.2017.05.018.

71. Wang, X.-Q., Tao, B.-B., Li, B., Wang, X.-H., Zhang, W.-C., Wan, L., Hua, X.-M., and Li, S.-T. (2016). Overexpression of TREM2 enhances glioma cell proliferation and invasion: a therapeutic target in human glioma. Oncotarget *7*, 2354–2366. https://doi.org/10.18632/oncotarget.6221.

72. Sun, R., Han, R., McCornack, C., Khan, S., Tabor, G.T., Chen, Y., Hou, J., Jiang, H., Schoch, K.M., Mao, D.D., et al. (2023). TREM2 inhibition triggers antitumor cell activity of myeloid cells in glioblastoma. Sci. Adv. *9*, eade3559. https://doi.org/10.1126/sciadv.ade3559.

73. Park-Min, K.-H., Ji, J.-D., Antoniv, T., Reid, A.C., Silver, R.B., Humphrey, M.B., Nakamura, M., and Ivashkiv, L.B. (2009). IL-10 Suppresses Calcium-Mediated Costimulation of Receptor Activator NF-κB Signaling during Human Osteoclast Differentiation by Inhibiting TREM-2 Expression. J. Immunol. *183*, 2444–2455. https://doi.org/10.4049/jimmunol.0804165.

74. Colonna, M., and Wang, Y. (2016). TREM2 variants: new keys to decipher Alzheimer disease pathogenesis. Nat. Rev. Neurosci. *17*, 201–207. https://doi.org/10.1038/nrn.2016.7.

75. Ennerfelt, H., Frost, E.L., Shapiro, D.A., Holliday, C., Zengeler, K.E., Voithofer, G., Bolte, A.C., Lammert, C.R., Kulas, J.A., Ulland, T.K., and Lukens, J.R. (2022). SYK coordinates neuroprotective microglial responses in neurodegenerative disease. Cell *185*, 4135–4152.e22. https://doi.org/10.1016/j.cell.2022.09.030.

76. Li, Y., Di, C., Song, S., Zhang, Y., Lu, Y., Liao, J., Lei, B., Zhong, J., Guo, K., Zhang, N., and Su, S. (2023). Choroid plexus mast cells drive tumor-associated hydrocephalus. Cell *186*, 5719–5738.e28. https://doi.org/10.1016/j.cell.2023.11.001.

77. Butler, A., Hoffman, P., Smibert, P., Papalexi, E., and Satija, R. (2018). Integrating single-cell transcriptomic data across different conditions, technologies, and species. Nat. Biotechnol. *36*, 411–420. https://doi.org/10.1038/nbt.4096.

78. Xing, X., Yang, F., Huang, Q., Guo, H., Li, J., Qiu, M., Bai, F., and Wang, J. (2021). Decoding the multicellular ecosystem of lung adenocarcinoma manifested as pulmonary subsolid nodules by single-cell RNA sequencing. Sci. Adv. *7*, eabd9738. https://doi.org/10.1126/sciadv.abd9738.

79. Puram, S.V., Tirosh, I., Parikh, A.S., Patel, A.P., Yizhak, K., Gillespie, S., Rodman, C., Luo, C.L., Mroz, E.A., Emerick, K.S., et al. (2017). Single-Cell Transcriptomic Analysis of Primary and Metastatic Tumor Ecosystems in Head and Neck Cancer. Cell *171*, 1611–1624.e24. https://doi.org/10.1016/j.cell.2017.10.044.

80. Tirosh, I., Izar, B., Prakadan, S.M., Wadsworth, M.H., 2nd, Treacy, D., Trombetta, J.J., Rotem, A., Rodman, C., Lian, C., Murphy, G., et al. (2016). Dissecting the multicellular ecosystem of metastatic melanoma by single-cell RNA-seq. Science *352*, 189–196. https://doi.org/10.1126/science.aad0501.

81. Guo, X., Zhang, Y., Zheng, L., Zheng, C., Song, J., Zhang, Q., Kang, B., Liu, Z., Jin, L., Xing, R., et al. (2018). Global characterization of T cells in non-small-cell lung cancer by single-cell sequencing. Nat. Med. *24*, 978–985. https://doi.org/10.1038/s41591-018-0045-3.

82. Speiser, D.E., Chijioke, O., Schaeuble, K., and Münz, C. (2023). CD4(+) T cells in cancer. Nat. Can. (Ott.) *4*, 317–329. https://doi.org/10.1038/s43018-023-00521-2.

83. Garcia-Alonso, L., Lorenzi, V., Mazzeo, C.I., Alves-Lopes, J.P., Roberts, K., Sancho-Serra, C., Engelbert, J., Marečková, M., Gruhn, W.H., Botting, R.A., et al. (2022). Single-cell roadmap of human gonadal development. Nature *607*, 540–547. https://doi.org/10.1038/s41586-022-04918-4.

84. Cannon, J.P., O'Driscoll, M., and Litman, G.W. (2012). Specific lipid recognition is a general feature of CD300 and TREM molecules. Immunogenetics *64*, 39–47. https://doi.org/10.1007/s00251-011-0562-4.

85. Chryplewicz, A., Scotton, J., Tichet, M., Zomer, A., Shchors, K., Joyce, J.A., Homicsko, K., and Hanahan, D. (2022). Cancer cell autophagy, reprogrammed macrophages, and remodeled vasculature in glioblastoma triggers tumor immunity. Cancer Cell *40*, 1111–1127.e9. https://doi.org/10.1016/j.ccell.2022.08.014.

86. Nalio Ramos, R., Missolo-Koussou, Y., Gerber-Ferder, Y., Bromley, C.P., Bugatti, M., Núñez, N.G., Tosello Boari, J., Richer, W., Menger, L., Denizeau, J., et al. (2022). Tissue-resident FOLR2+ macrophages associate with CD8+ T cell infiltration in human breast cancer. Cell *185*, 1189–1207.e25. https://doi.org/10.1016/j.cell.2022.02.021.

87. Kleinberger, G., Yamanishi, Y., Suárez-Calvet, M., Czirr, E., Lohmann, E., Cuyvers, E., Struyfs, H., Pettkus, N., Wenninger-Weinzierl, A., Mazaheri, F., et al. (2014). TREM2 mutations implicated in neurodegeneration impair cell surface transport and phagocytosis. Sci. Transl. Med. *6*. https://doi.org/10.1126/scitranslmed.3009093.

Please cite this article in press as: Zhong et al., Distinct roles of TREM2 in central nervous system cancers and peripheral cancers, Cancer Cell (2024), https://doi.org/10.1016/j.ccell.2024.05.001

STAR★METHODS

KEY RESOURCES TABLE

REAGENT or RESOURCE	SOURCE	IDENTIFIER
Antibodies		
anti-human TREM2	Abcam	Cat# ab209814; RRID: AB_3095849; clone EPR20243
anti-Flag	Sigma Aldrich	Cat# F1804; RRID: AB_262044; clone M2
anti-β-tubulin	CST	Cat# 2128; RRID: AB_823664; clone 9F3
anti-mouse TREM2	CST	Cat# 55739; RRID: AB_3095850; clone E4J7A
anti-CD206/MRC1	Boster	Cat# A02285; RRID: AB_3081542
anti-ARG1	Proteintech	Cat# 16001-1-AP; RRID: AB_2289842
anti-human iNOS	Boster	Cat# A00368; RRID: AB_3081084
anti-mouse iNOS	Santa Cruz	Cat# sc-7271; RRID: AB_627810; clone C-11
anti-HLA-DR	BioLegend	Cat# 307602; RRID: AB_314680; clone L243
anti-pSTAT3	CST	Cat# 9145; RRID: AB_2491009; clone D3A7
anti-STAT3	BOSTER	Cat# BM4052; RRID: AB_3095851
anti-pSTAT1	CST	Cat# 9167; RRID: AB_561284; clone 58D6
anti-STAT1	BOSTER	Cat# BM4110; RRID: AB_3095852
anti-pSYK	CST	Cat# 2717; RRID: AB_2218658; clone 65E4
anti-pSYK	Abcam	Cat# ab300398; RRID: AB_3095853; clone EPR26232-39
anti-SYK	Proteintech	Cat# 66721-1-Ig; RRID: AB_2882072; clone 4C4A12
anti-pAKT2 Ser474	CST	Cat# 8599; RRID: AB_2630347; clone D3H2
anti-AKT2	CST	Cat# 5239; RRID: AB_10544406; clone L79B2
anti-GAPDH	SAB	Cat# 21612; RRID: AB_10760516
anti-pAKT1 Ser473	CST	Cat# 9018; RRID: AB_2629283; clone D7F10
anti-AKT1	CST	Cat# 75692; RRID: AB_2716309; clone D9R8K
anti-pAKT Ser473	SAB	Cat# 11054; RRID: AB_894814
anti-pan AKT	Boster	Cat# BM4400; RRID: AB_3095854
Anti-MHC class II (I-A/I-E)	Millipore	Cat# MABF33; RRID: AB_11211014; clone M5/114
anti-human IBA1	Proteintech	Cat# 66827-1-Ig; RRID: AB_2882170; clone 1C6A10
anti-human TREM2	R&D	Cat# MAB17291; RRID: AB_2208679; clone 237920
anti-mouse IBA1	Servicebio	Cat# GB12105; RRID: AB_2922434
anti-mouse TREM2	R&D	Cat# AF1729; RRID: AB_354956
Dylight 488, Goat Anti-Rat IgG	Abbkine	Cat# A23240; RRID: AB_3095855
Donkey anti-Mouse IgG (H + L) Highly Cross-Adsorbed Secondary Antibody, Alexa Fluor™ 594	Invitrogen	Cat# A21203; RRID: AB_141633
Goat anti-Rabbit IgG (H + L) Highly Cross-Adsorbed Secondary Antibody, Alexa Fluor™ Plus 488	Invitrogen	Cat# A32731; RRID: AB_2633280
Brilliant Violet 711 anti-mouse CD3	BioLegend	Cat# 100241; RRID: AB_2563945; clone 17A2
APC anti-mouse NK-1.1	BioLegend	Cat# 108710; RRID: AB_313396; clone PK136
Brilliant Violet 510 anti-mouse/human CD11b	BioLegend	Cat# 101263; RRID: AB_2629529; clone M1/70
Brilliant Violet 421 anti-mouse F4/80	BioLegend	Cat# 123137; RRID: AB_2563102; clone BM8
BUV395 anti-mouse Ly-6G	BD Biosciences	Cat# 565964; RRID: AB_2739417; clone 1A8
PE/Dazzle 594 anti-mouse CD11c	BioLegend	Cat# 117347; RRID: AB_2563655; clone N418
BUV395 Rat Anti-mouse CD3	BD Biosciences	Cat# 569614; RRID: AB_3095858; clone 17A2
Brilliant Violet 510 anti-mouse CD4	BioLegend	Cat# 100449; RRID: AB_2564587; clone GK1.5

(*Continued on next page*)

Please cite this article in press as: Zhong et al., Distinct roles of TREM2 in central nervous system cancers and peripheral cancers, Cancer Cell (2024), https://doi.org/10.1016/j.ccell.2024.05.001

Continued

REAGENT or RESOURCE	SOURCE	IDENTIFIER
Brilliant Violet 711 anti-mouse/human B220	BioLegend	Cat# 103255; RRID: AB_2563491; clone RA3-6B2
APC/Cyanine7 anti-mouse CD8a	BioLegend	Cat# 100714; RRID: AB_312753; clone 53-6.7
PE/Cyanine5 anti-mouse/human CD44	BioLegend	Cat# 103010; RRID: AB_312961; clone IM7
Alexa Fluor 647 anti-mouse CD62L	BioLegend	Cat# 104421; RRID: AB_493379; clone MEL-14
PE-Cyanine7 anti-mouse IFN gamma	BioLegend	Cat# 505825; RRID: AB_1595591; clone XGM1.2
Brilliant Violet 650 anti-mouse CD279 (PD-1)	BD Biosciences	Cat# 744546; RRID: AB_2742317; clone J43
APC anti-mouse CD223 (LAG-3)	BioLegend	Cat# 125210; RRID: AB_10639727; clone C9B7W
APC anti-mouse Arginase 1	eBioscience	Cat# 17-3697-82; RRID: AB_2734835; clone A1exF5
PE anti-mouse iNOS	eBioscience	Cat# 12-5920-82; RRID: AB_2572642; clone CXNFT
Brilliant Violet 605 anti-mouse CD206	BioLegend	Cat# 141721; RRID: AB_2562340; clone C068C2
Brilliant Violet 785 anti-mouse PD-L1	BioLegend	Cat# 124331; RRID: AB_2629659; clone 10F.9G2
Brilliant Violet 711 anti-mouse CD11c	BioLegend	Cat# 117349; RRID: AB_2563905; clone N418
Alexa Fluor 647 anti-human/mouse TREM2	R&D	Cat# FAB17291R; RRID: AB_3095857; clone237920
Brilliant Violet 785 anti-mouse CD86	BioLegend	Cat# 105043; RRID: AB_2566722; clone GL-1
PE/Dazzle 594 anti-human/mouse Granzyme B	BioLegend	Cat# 372216; RRID: AB_2728383; clone QA16A02
Alexa Fluor 700 anti-mouse CD45	BioLegend	Cat# 103128; RRID: AB_493715; clone 30-F11
PerCP/Cyanine5.5 anti-mouse Ly-6C	BioLegend	Cat# 128012; RRID: AB_1659241; clone HK1.4
PE anti-mouse NK-1.1	BioLegend	Cat# 108707; RRID: AB_313394; clone PK136
APC/Cyanine7 anti-human CD14	BioLegend	Cat# 325620; RRID: AB_830693; clone HCD14
PerCP/Cyanine5.5 anti-human CD16	BioLegend	Cat# 302028; RRID: AB_893262; clone 3G8
PE anti-human CD49d	BioLegend	Cat# 304304; RRID: AB_314430; clone 9F10
BV605 anti-mouse CD25	BioLegend	Cat# 102036; RRID: AB_2563059; clone PC61
APC anti-mouse Perforin	BioLegend	Cat# 154304; RRID: AB_2721463; clone S16009A
PE/Dazzle 594 anti-mouse TNF-α	BioLegend	Cat# 506346; RRID: AB_2565955; clone MP6-XT22
Brilliant Violet 785 anti-mouse CD11c	BioLegend	Cat# 117335; RRID: AB_11219204; clone N418
Brilliant Violet 711 anti-mouse TCRβ	BioLegend	Cat# 109243; RRID: AB_2629564; clone H57-597
APC anti-mouse CD19	BioLegend	Cat# 115511; RRID: AB_313646; clone 6D5
Alexa Fluor 488 anti-mouse CD4	BioLegend	Cat# 100425; RRID: AB_493520; clone GK1.5
BV605 anti-mouse CD8	BioLegend	Cat# 100743; RRID: AB_2561352; clone 53-6.7
PE/Cyanine5 anti-mouse CD80	BioLegend	Cat# 104712; RRID: AB_313133; clone 16-10A1
PE/Cyanine7 anti-mouse CD163	BioLegend	Cat# 155320; RRID: AB_2890710; clone S15049I
Biological samples		
Human glioma specimen	Department of Neurosurgery, the First Affiliated Hospital of Sun Yat-sen University	N/A
Human cerebrospinal fluid specimen	Department of Neurosurgery, the First Affiliated Hospital of Nanjing Medical University	N/A
Chemicals, peptides, and recombinant proteins		
$OVA_{257-264}$(SIINFEKL) peptide	Solarbio	Cat# CLP0080
IA9 and IA9-FITC peptide	Botai Biotechnology	N/A
Sphingomyelin	Macklin	Cat# S929003
Ganglioside GM1	Macklin	Cat# G873919
Tamoxifen	Sigma Aldrich	Cat# T5648; CAS#10540-29-1
Corn Oil	Macklin	Cat# C805618; CAS#8001-30-7
Debris Removal Solution	Miltenyi Biotec	Cat# 130-109-398
Carboxyfluorescein Succinimidyl Ester (CFSE)	BD Biosciences	Cat# 565082
CD3/CD28 Dynabeads	Thermo Fisher	Cat# 11456D

(*Continued on next page*)

Please cite this article in press as: Zhong et al., Distinct roles of TREM2 in central nervous system cancers and peripheral cancers, Cancer Cell (2024), https://doi.org/10.1016/j.ccell.2024.05.001

Continued

REAGENT or RESOURCE	SOURCE	IDENTIFIER
pHrodo *E. coli* Bioparticles	Thermo Fisher	Cat# P35361
Evo M-MLV RT Master Mix	Accurate Biology	Cat# AG11706
SYBR Green *Pro Taq* HS Premix	Accurate Biology	Cat# AG11718
Cell Stimulation Cocktail	Thermo Fisher	Cat# 00-4975-93
Fixable Viability Dye eFluor 520/455UV	Thermo Fisher	Cat# 65-0867-14/65-0868-14
Sodium Citrate Buffer	Beyotime	Cat# P0081
Critical commercial assays		
Arginase Activity Assay Kit	Solarbio	Cat# BC5555
Enhanced BCA Protein Assay Kit	Beyotime	Cat# P0010
Foxp3/Transcription Factor Staining Buffer Set	Thermo Fisher	Cat# 00-5523-00
Tumor Dissociation Kit, mouse	Miltenyi Biotec	Cat# 130-096-730
Tumor Dissociation Kit, human	Miltenyi Biotec	Cat# 130-095-929
MojoSort Human CD14 Selection Kit	BioLegend	Cat# 480026
MojoSort Mouse CD8 T cell Isolation Kit	BioLegend	Cat# 480008
MojoSort Mouse CD3 T cell Isolation Kit	BioLegend	Cat# 480024
EasySep Direct Human T cell Isolation Kit	StemCell	Cat# 19661
Deposited data		
ScRNA-seq datasets of mouse TREM2-wildtype or deficient models	this paper	GSA: CRA012254
ScRNA-seq datasets of mouse vector- or AAV-TREM2-treated models	this paper	GSA: CRA014760
RNA-seq datasets of sorted murine myeloid cells from intracranial and subcutaneous tumor models	this paper	GSA: CRA012271
ScRNA-seq datasets of early stage or late-stage murine GBM models	this paper	GSA: CRA014718
SnRNA-seq datasets of spontaneous GBM mouse model	this paper	GSA: CRA012090
ScRNA-seq datasets of human glioma samples	this paper	GSA-Human: HRA005318
Spatial sequencing datasets of human glioma samples	this paper	GSA-Human: HRA005322
RNA-seq and survival data of human glioma samples	OncoInc	TCGA RNAseqV2
RNA-seq and survival data of human glioma samples	PrognoScan	GEO: GSE7696
RNA-seq and survival data of human glioma samples	Chinese Glioma Genome Atlas	mRNAseq693
TCGA Clinical Data Resource	Liu et al. 2018[51]	N/A
Experimental models: Cell lines		
GL261	DSMZ	Cat# ACC802
CT-2A	Millipore	Cat# SCC194
EO771	Meisen CTCC	Cat# 003–0098
Experimental models: Organisms/strains		
Mouse: *Trem2*$^{-/-}$ mice: C57BL/6JSmoc-*Trem2*^{em1Smoc}	Model Organisms	Cat# NM-KO-190402
Mouse: littermate *Trem2*$^{+/+}$ mice	Model Organisms	N/A
Mouse: C57BL/6J	The Laboratory Animal Center of the First Affiliated Hospital of Sun Yat-sen University	N/A

(*Continued on next page*)

Please cite this article in press as: Zhong et al., Distinct roles of TREM2 in central nervous system cancers and peripheral cancers, Cancer Cell (2024), https://doi.org/10.1016/j.ccell.2024.05.001

Continued

REAGENT or RESOURCE	SOURCE	IDENTIFIER
Mouse: spTREM2-WT: *Gfap-Cre; Trp53$^{f/f}$; R26-MET404-flag$^{LSL/+}$*	Prof. ZHANG Nu's Lab, Zhong et al., 2023	N/A
Mouse: spTREM2-KO: *Trem2$^{-/-}$; Gfap-Cre; Trp53$^{f/f}$; R26-MET404-flag$^{LSL/+}$*	Model Organisms	N/A
Mouse: OT-1 mice: C57BL/6-Tg (TcraTcrb)1100Mjb/J	The Jackson Laboratory	Cat# 003831
Mouse: *Trem2$^{f/f}$*: C57BL/6JCya-*Trem2^{em1flox}*/Cya	Cyagen	Cat# S-CKO-17045
Mouse: *Tmem119^{CreER}*: Tmem119-2A-CreERT2	Cyagen	Cat# C001327
Mouse: *Ccr2^{Cre}*	Prof. BIAN Xiuwu and Dr. SHI Yu's Lab	N/A
Mouse: *Tmem119^{CreER};Trem2 $^{f/f}$*	Cyagen	N/A
Mouse: *Ccr2^{Cre};Trem2 $^{f/f}$*	Cyagen	N/A
Oligonucleotides		
Primers: see Table S6		
Recombinant DNA		
AAV9-F4/80-MCS-p2A-GFP	WZ Biosciences	N/A
AAV9-F4/80-TREM2-flag-p2A-GFP	WZ Biosciences	N/A
Software and algorithms		
R (version 4.2.2)	The R Foundation	https://www.r-project.org/
Cell Ranger (version 6.1.2)	10x Genomics	https://10xgenomics.com/
Seurat Package (version 4.1.0)	Satija Lab and collaborators	https://satijalab.org/seurat/
CellphoneDB (version 4)	Lorenzi et al., 2022	https://www.cellphonedb.org
Space Ranger (version 1.3.1)	10x Genomics	https://10xgenomics.com/
SPATA2 package (version 2.0.4)	Kueckelhaus Lab and collaborators	https://themilolab.github.io/SPATA2/index.html
GraphPad Prism (version 9.5.0)	GraphPad	https://www.graphpad.com
SkanIt (version 6.1)	Thermo Fisher	https://www.thermofisher.com
Excel (version 16.80)	Microsoft	https://www.microsoft.com
FlowJo (version 10.6.2)	FlowJo, LLC	https://www.flowjo.com
GEPIA	Tang et al. 2017	http://gepia.cancer-pku.cn/

RESOURCE AVAILABILITY

Lead contact

Further information and requests for resources and reagents should be directed to and will be fulfilled by the lead contact, Nu Zhang (zhangnu2@mail.sysu.edu.cn).

Materials availability

All stable and unique reagents generated in this study are available from the lead contact upon reasonable request.

Data and code availability

Raw data of the murine scRNA-seq, single-nucleus RNA sequencing (snRNA-seq), bulk RNA-seq of sorted myeloid cells from intracranial and subcutaneous tumor models have been deposited in the Genome Sequence Archive (GSA) in National Genomics Data Center (NGDC). Raw data of the human GBM scRNA-seq and human GBM spatial transcriptomics have been deposited in the GSA-human database in NGDC. The data are publicly available as of the date of publication. Accession numbers are listed in the key resources table. This paper does not report original code. Any additional information required to reanalyze the data reported in this paper is available from the lead contact upon request.

Please cite this article in press as: Zhong et al., Distinct roles of TREM2 in central nervous system cancers and peripheral cancers, Cancer Cell (2024), https://doi.org/10.1016/j.ccell.2024.05.001

EXPERIMENTAL MODEL AND STUDY PARTICIPANT DETAILS

Human tissues and blood samples

Human glioma cancerous and peritumor tissues and peripheral blood samples were collected at the Department of Neurosurgery of the First Affiliated Hospital of Sun Yat-sen University with informed consent from the donors. The pathological features of the analyzed samples were confirmed by neuropathologists. The study was approved by the Ethics Institutional Review Boards of the First Affiliated Hospital of Sun Yat-sen University and complied with all relevant ethical regulations regarding human participants. The cerebrospinal fluid samples of GBM patients and control patients (without tumors and CNS disorders) were collected at the Department of Neurosurgery of the First Affiliated Hospital of Nanjing Medical University with informed consent from the donors and the sample collection was approved by the Ethics Committee of the First Affiliated Hospital of Nanjing Medical University.

Cell lines

The murine glioma cell lines GL261 and CT-2A were purchased from the Leibniz Institute DSMZ-German Collection of Microorganisms and Cell Cultures GmbH (ACC 802) and Millipore (SCC194), respectively. The murine breast cancer cell line EO771 was obtained from Meisen CTCC (003–0098). These cell lines were maintained in DMEM (Gibco) supplemented with 10% fetal bovine serum (FBS), cultured in a humidified incubator at 37°C with 5% CO_2 and were regularly tested and verified to be free of mycoplasma contamination.

Mouse strains and housing

C57BL/6J mice were purchased from the Laboratory Animal Center of the First Affiliated Hospital of Sun Yat-sen University. *Trem2*$^{-/-}$ mice (C57BL/6JSmoc-*Trem2*^{em1Smoc}, #NM-KO-190402) and littermate wild-type mice (C57BL/6J) were obtained from Model Organisms (Shanghai, China). Briefly, Cas9 mRNA and gRNAs (gRNA1: CGCTATGCTCCCTGCACTCCTGG; gRNA2: CTGGCAGTGA CTGCGGATGGAGG) were microinjected into the fertilized eggs of C57BL/6J mice, and the injected fertilized eggs were transplanted into pseudopregnant female mice. The mice born afterward were F0 generation mice. The F0 generation mice identified as positive by PCR amplification and Sanger sequencing were further mated with C57BL/6J mice to obtain F1 generation mice (target mice) with stable inheritance. Spontaneous genetic GBM mouse models (spTREM2-WT: *Gfap-Cre; Trp53*$^{f/f}$*; R26-MET404-flag*$^{LSL/+}$; spTREM2-KO: *Trem2*$^{-/-}$*; Gfap-Cre; Trp53*$^{f/f}$*; R26-MET404-flag*$^{LSL/+}$) were generated by Model Organisms. The spTREM2-WT mice have been validated in a previous report.[35] OT-1 mice were obtained from the Jackson Laboratory (#003831). *Trem2* $^{f/f}$ mice (CKO-control, #S-CKO-17045, Cyagen) were crossed with *Tmem119*^{CreER} (Tmem119-2A-CreERT2, #C001327, Cyagen) and *Ccr2*^{Cre} mice (kindly provided by Prof. BIAN Xiuwu and Dr. SHI Yu's Lab) to generate *Tmem119*^{CreER}*;Trem2*$^{f/f}$ and *Ccr2*^{Cre}*;Trem2*$^{f/f}$ mice, respectively. Three weeks prior to tumor initiation, the mice for CKO experiments were intraperitoneally injected with 100 mg/mL tamoxifen (dissolved in corn oil) for 5 consecutive days. The mice were kept in specific-pathogen-free (SPF) status under a 12-h light-dark cycle at 24°C–26°C and 50–70% humidity. All of the animal experiments conducted in this study were approved by the Ethics Institutional Review Boards of the First Affiliated Hospital of Sun Yat-sen University.

METHOD DETAILS

Tumor models

To establish orthotopic brain tumor models, eight-week-old mice were anesthetized with isoflurane. The mice were then intracranially injected with GL261, CT-2A or EO771 cells (1.0×10^5) in 2.5 μL PBS with a 10-μL Hamilton syringe through a guide screw into the right frontal lobe at a depth of 2.5 mm. For the metastatic brain tumor model in Figure S7, EO771 cells (4.0×10^5) were injected into the internal carotid artery of the mice.[76] For the extracranial tumor model, GL261 (2.0×10^6) cells resuspended in 100 μL PBS were subcutaneously injected into the flank of each mouse. For *in vivo* TREM2 signaling blocking, the blocking peptide IA9 (25 mg/kg)[36] was resolved in DMSO and diluted in 200 μL PBS, and was intraperitoneally injected into the mice daily from day 7 after intracranial tumor inoculation until the mice were sacrificed. For *in vivo* TREM2 overexpression, AAV-TREM2 (~5.0×10^{10} VG/mL in 2 μL per mouse) or control vector was intracranially injected on day 3 and day 10 after GL261/CT-2A inoculation. For ICB, mice were intracranially injected with anti-PD-1 antibody (BE0146, BioXcell, 10 mg/kg, 1:5 diluted in PBS) or IgG control antibody every 5 days after tumor inoculation. The mice were monitored and weighed every day and humanely sacrificed once they displayed neurological symptoms, 20% weight loss or became moribund. The intracranial tumor volume (mm^3) was calculated by measuring the length (L) and width (W) of the tumor from the HE-stained sections ($V = \pi/6*L*W^2$). For the subcutaneous tumor model, the tumor size was routinely measured, and the mice were euthanized when the tumor volume reached ~1000 mm^3.

Bioinformatic analysis

Single-cell RNA-seq data processing

Raw gene expression matrices were generated for each sample by Cell Ranger (version 6.1.2) pipeline coupled with the human reference genome version GRCh38 and the mouse reference genome version mm10, respectively. The output filtered gene expression matrices were analyzed by the Seurat package (version 4.1.0).[77] In brief, genes expressed at a proportion >0.1% of the data and cells with >200 genes detected were selected for further analyses. For human data, low-quality cells were removed if they met the following criteria: 1) $\leq$ 500 genes, 2) $\geq$ 8,000 genes, 3) $\geq$ 50,000 UMIs or 4) $\geq$ 10% UMIs derived from the mitochondrial genome.

For murine data, low-quality cells were removed if they met the following criteria: 1) $\leq$ 200 genes, 2) $\geq$ 8,000 genes, 3) $\geq$ 50,000 UMIs or 4) $\geq$ 10% UMIs derived from the mitochondrial genome. After removal of low-quality cells, the gene expression matrices were normalized by the *NormalizeData* function, and 2000 features with high cell-to-cell variation were calculated using the *FindVariableFeatures* function. To reduce the dimensionality of the datasets, the *RunPCA* function was conducted with default parameters on linear-transformation scaled data generated by the *ScaleData* function. Next, the *ElbowPlot*, *DimHeatmap* and *JackStrawPlot* functions were used to identify the true dimensionality of each dataset, as recommended by the Seurat developers. Finally, we clustered cells using the *FindNeighbors* and *FindClusters* functions and performed nonlinear dimensional reduction with the *RunUMAP* function with default settings. All details regarding the Seurat analyses performed in this work can be found in the website tutorial [https://satijalab.org/seurat/articles/get_started.html].

Multiple dataset integration

To compare cell types and proportions between the wild-type and *Trem2*$^{-/-}$ mice, the Seurat package was used to assemble multiple distinct scRNA-seq datasets into an integrated and unbatched dataset. In brief, we identified 2000 features with high cell-to-cell variation as described above. Next, we identified "anchors" between individual datasets with the *FindIntegrationAnchors* function and input these anchors into the *IntegrateData* function to create a "batch-corrected" expression matrix of all cells, which allowed cells from different datasets to be integrated and analyzed together.

Cell type annotation and cluster marker identification

After nonlinear dimensional reduction and projection of all cells into two-dimensional space by UMAP, cells were clustered together according to common features. The *FindAllMarkers* function in Seurat was used to find markers for each of the identified clusters. Clusters were then classified and annotated based on the expression of canonical markers of particular cell types. Clusters expressing two or more canonical cell-type markers were classified as doublet cells and excluded from further analysis.

Subclustering of major cell types

To characterize the subsets of a major cell type, cells from that major cell type were first extracted from the overview integrated dataset first. Next, the cells from this major cell type were integrated for further subclustering. After integration, genes were scaled to unit variance. Scaling, PCA, and clustering were performed as described above.

DEG identification and functional enrichment

Differential gene expression testing was performed using the FindMarkers function in Seurat with parameter 'test.use = wilcox' by default. DEGs were filtered using a minimum $\log_2$(fold change) of 0.2 and a maximum *p*-value of 0.01. Enrichment analysis for the functions of the DEGs was conducted using the Metascape webtool (www.metascape.org). Gene sets were derived from the Molecular Signatures Database (MSigDB) (https://www.gsea-msigdb.org/gsea/msigdb), including the following collections of gene sets: GO Biological Processes, Hallmark Gene Sets, Reactome Gene Sets, WikiPathways, KEGG Pathway, and PANTHER Pathway.

Defining cell state scores

We used cell scores to evaluate the degree to which individual cells expressed a certain predefined expression gene set.[78–81] The cell scores were initially based on the average expression of the genes from the predefined gene set in the respective cell. For a given cell i and a gene set j (Gj), the cell score SCj(i) quantifies the relative expression of Gj in cell i as the average relative expression (Er) of the genes in Gj compared to the average relative expression of a control gene set (Gjcont): SCj(i) = average[Er(Gj, i)] – average[Er(Gjcont, i)]. The control gene set was randomly selected based on aggregate expression level bins, which yielded a comparable distribution of expression levels and over size to that of the considered gene set. The *AddModuleScore* function in Seurat was used to implement the method with default settings. We used well-defined naive markers (*Ccr7, Sell, Lef1,* and *Tcf7*), effector-associated genes (*Prf1, Ifng, Nkg7, Gzmb, Gzma, Gzmk, Gzmd, Klrk1, Klrb1, Klrd1, Ctsw,* and *Cst7*), exhaustion markers (*Pdcd1, Tigit, Ctla4, Havcr2, Tox,* and *Cd244a*) and T cell helper markers (*Ifng, Tnf, Il2, Il2ra, Il4, Il6, Il17a, Il21, Il22, Cd69, Cd74, H2-Aa*) to define the naive, effector, exhaustion and helper scores of the T cells.[78,81,82] The monocyte and macrophage signature scores were measured on 10 monocyte marker genes (*Ly6c2, Plac8, Chil3, Hp, Ccr2, Gsr, Plaur, Cebpb, Taldo1,* and *Klra2*), and 9 macrophage maker genes (*Apoe, C1qa, C1qc, Ms4a7, Cd81, Egr1, Itm2b, Tmem176a,* and *Tmem176b*), respectively.

Putative cell-to-cell interaction patterns

We calculated the expression of ligand-receptor pairs between any two cell types across conditions to infer intercellular communication by CellphoneDB (version 4).[83] Mouse gene names were translated to their human orthologs first. Next, the statistical analysis method was employed with default parameters based on interactions and complexes database version 4.0.0. All details regarding the interaction analyses performed in this work can be found on the official website [https://cellphonedb.readthedocs.io/en/latest/index.html]. Ktplots [https://github.com/zktuong/ktplots] (version 2.3.0) was used to enhance the visualization of CellPhoneDB results.

Spatial transcriptomics visium data analysis

Raw gene expression matrices were generated for each sample by Space Ranger (version 1.3.1) pipeline coupled with the human reference genome version GRCh38. The output filtered gene expression matrices were analyzed by the SPATA2 package (version 2.0.4). In brief, the initiateSpataObject_10X function was employed to create a spata2 object and perform a variety of computations (e.g., count normalization, dimensionality reduction and clustering) while relying on the gold-standard functions of the Seurat-package. Then, spatial trajectories were added to the spata2 object via two functions, createSpatialTrajectory and addSpatialTrajectory. Copy number variation (CNV) analysis of spatial data is implemented in SPATA2 through the runCnvAnalysis command. We measured the mean expression levels of the genes in BP.GO_NEGATIVE_REGULATION_OF_MYELINATION, HM_INFLAMMATORY_RESPONSE to define the myelin sheath (MS) degradation and inflammatory stress, respectively. All details

regarding the SPATA2 analyses performed in this work can be found on the website [https://themilolab.github.io/SPATA2/index.html].

RNA-seq analysis

Paired-end read sequences were aligned to the mouse reference genome (version mm10) using the default settings in STAR (version 2.6.1b) and quantified by HTSeq (version 0.11.0) in "intersection-strict" mode. Significant DEGs were identified as those with a false discovery rate (FDR) value above the threshold ($Q < 0.05$) and fold-change >2 using edgeR software (v3.2.0). To assign pathway activity estimates to individual samples, we applied GSVA (version 1.40.1) using standard settings for KEGG metabolism pathways as described previously.[78] The differential activity levels of pathways between conditions were calculated using Limma (version 3.48.1). Each pathway with a Benjamini-Hochberg-corrected p value <0.05 and absolute t-value >2.5 was considered to be significantly disturbed. GSEA was conducted using the fgseaMultilevel function in the fgsea package.

Metabolomics analysis

Collected CSF samples were subjected to global metabolomics profiling using an ultrahigh-performance liquid chromatography–mass spectrometry (UPLC–MS/MS) platform following conventional metabolomics procedures (MetWare Biotechnology Inc.). Significantly regulated lipids between the normal CSF and the GBM CSF groups were determined by VIP ≥ 1 and absolute Log2FC (fold change) $\geq$ 1. VIP values were extracted from the OPLS-DA results generated using the R package MetaboAnalystR. The data were log transformed (log2) and mean centered before OPLS-DA. To avoid overfitting, a permutation test (200 permutations) was performed. Identified lipids were annotated using the KEGG compound database. Pathway enrichment analysis was carried out following instructions from online tool MetaboAnalyst [https://www.metaboanalyst.ca].

Public database analysis

Survival data of three GBM cohorts in TCGA RNAseqV2, GSE7696 and mRNAseq_693 datasets were obtained from Oncolnc [http://www.oncolnc.org/], PrognoScan [http://dna00.bio.kyutech.ac.jp/PrognoScan/] and the CGGA database [http://www.cgga.org.cn/index.jsp]. The data were analyzed and illustrated by GraphPad Prism (version 9.5.0). The expression of TREM2 in the cohorts from TCGA and GTEx datasets was plotted following the instructions provided by the online tool GEPIA [http://gepia.cancer-pku.cn/]. The clinical relevance of TREM2 negatively regulated genes in GBM was investigated using the standardized dataset named the TCGA Pan-Cancer Clinical Data Resource (TCGA-CDR).[51] GBM patients were classified into high and low groups based on the optimal cutpoint returned by the surv_cutpoint function.

Constructs and reagents

The TREM2-overexpressing (AAV9-F4/80-TREM2-flag-p2A-GFP) and the control (AAV9-F4/80-MCS-p2A-GFP) adeno-associated viruses were generated by WZ Biosciences. TREM2 blocking 9-mer peptide IA9 or IA9-FITC was synthesized, purified and validated by mass spectrometry according to the reported protocols[36] by Botai Biotechnology (Shanghai, China). Sphingomyelin (S929003, Macklin) and ganglioside GM1 (G873919, Macklin) were purchased from Macklin, China. Purified lipids were dissolved in methanol, coated onto high-absorbent plates (Thermo Fisher), and incubated at room temperature to dry for 15 min in a biological safety cabinet prior to downstream stimulation experiments, as previously reported.[4,84]

Cell suspension preparation and cell sorting

Fresh human or mouse tissues were cut into 2-4 mm pieces and transferred into gentleMACS C tubes (130-093-237, Miltenyi Biotec). Tissues were digested in an enzyme mix (130-096-730 for mouse and 130-095-929 for human tissues, Miltenyi Biotec) on a gentleMACS Octo Dissociator following the manufacturer's protocols. The cell suspension was diluted in PBS and filtered through 70 μm strainers. Cell debris was excluded by Debris Removal Solution (130-109-398, Miltenyi Biotec) according to the manufacturer's instructions. Red blood cells (RBC) were then removed using RBC lysis buffer (C3702, Beyotime). The cell pellets were then resuspended in FACS staining buffer (PBS +2% FBS) and ready for downstream experiments (scRNA-seq, flow cytometry or magnetic sorting, etc.). $CD14^+$ cells from human brain tissues were sorted by a magnetic isolation kit (480026, BioLegend) following the manufacturer's protocols.

Isolation of TAMs from tumor samples

Fresh mouse or human tumor tissues were digested into single-cell suspensions using the abovementioned methods. The cell suspension was then subjected to flow cytometry cell sorting using previously reported gating strategies.[16,63] For the mouse tissues, TAMs were defined as live $CD45^+CD11b^+F4/80^+LY6C^-LY6G^-$ cells (including both MDMs and MG for GBM samples). For human GBM tissues, TAMs were defined as live $CD45^+CD11b^+CD14^+CD16^-$ cells (including both MDMs and MG). The sorted cells were resuspended in collection medium (RPMI 1640 + 10% FBS) and used for downstream analysis.

Arginase activity assessment

TAMs were isolated from GL261-GBM-bearing mice using abovementioned methods. After cell counting, the same number of TAMs (2.0×10^5) from each group was subjected to an arginase activity assay (BC5555, Solarbio) following the manufacturer's instructions. The absorbance was measured at 560 nm, and the arginase activity was calculated and normalized using SkanIt software (version 6.1) and Microsoft Excel (version 16.80).

Please cite this article in press as: Zhong et al., Distinct roles of TREM2 in central nervous system cancers and peripheral cancers, Cancer Cell (2024), https://doi.org/10.1016/j.ccell.2024.05.001

T cell isolation and T cell suppression assay

For separating murine primary T cells, mouse spleens were collected and crushed by the plunger end of a syringe. The splenocytes were washed through a 70 μm cell strainer and incubated in RBC lysis buffer (C3702, Beyotime) to remove red blood cells. $CD3^+$ T or $CD8^+$ T cells were then magnetically isolated from the cells by MojoSort Mouse $CD3^+$ T cell Isolation Kit (480024, BioLegend) or by MojoSort Mouse $CD8^+$ T cell Isolation Kit (480008, BioLegend). For separating human $CD3^+$ T cells from peripheral whole blood, an EasySep Direct Human T cell Isolation Kit (19661, StemCell) was applied following the manufacturer's instructions. The isolated T cells were first labeled with 1 μM carboxyfluorescein succinimidyl ester (CFSE, 565082, BD Biosciences), activated with CD3/CD28 Dynabeads[85] (11456D, Thermo Fisher) and plated with the myeloid cells at a ratio of 1:1. In some instances, the myeloid cells were incubated with the indicated lipids 24 h prior to coculture. After 72 h of coculture, the cells were stained with indicated antibodies and Fixable Viability Dye eFluor 455UV (65-0868-14, eBioscience).

T cell priming assay

This assay was performed following a previously published method.[86] Briefly, the sorted TAMs were incubated with the $OVA_{257-264}$ (SIINFEKL) peptide (1 nM) for 1 h at 37°C and cocultured with CFSE-labeled OT-1 $CD8^+$ T cells (separated from the spleens of OT-1 mice). After 72 h of coculture, the cells were stained for CD8, CD44, CD25, CD62L and PD-1 to analyze their activation status.

Phagocytosis assay

The assay was conducted based on previously published methods.[87] Briefly, cells were seeded at a density of $\sim 2\times10^5$ in 24-well plates coated with purified lipids or control solvent and incubated for 24 h pHrodo *E. coli* bioparticles (P35361, Invitrogen) at a concentration of 1 μg/μL were prepared in PBS, and a total of 50 μg of bioparticles was added per well. A negative control sample containing all reagents was incubated on ice, according to the manufacturer's protocol. After incubation for 60 min at 37°C, cells were harvested and washed two times with FACS staining buffer (PBS +2% FBS), and analyzed by a BD FACS Celesta flow cytometer. Data analysis was performed using the FlowJo software (version 10.6.2).

Microglial depletion

To pharmacologically deplete the MG in the mouse brain, mice were fed with PLX3397-formulated AIN-76A diet (290 ppm, Moldiets) or control AIN-76A diet daily.[40] Twenty-one days after the initial feeding, the mice were intracranially inoculated with GL261 cells. The feeding treatment was maintained until the mice were sacrificed. Blood samples for investigating the impact on peripheral monocytes were collected from the submandibular vein.

Reverse transcription and qPCR

RNA reverse transcription was performed using *Evo M-MLV* RT Master Mix (AG11706, Accurate Biology). Then, qPCR was conducted using SYBR Green *Pro Taq* HS Premix (AG11718, Accurate Biology) in a QuantStudio 5 system (Applied Biosystems). Primers are summarized in Table S6.

Reporter assay

GFP-NFAT reporter cells[4] were stably transfected with human TREM2 and DAP12 cDNAs. The reporter cells were added to the wells coated with purified lipids or treated with solvent. The reporter activity (%) was assessed after overnight incubation, which is defined as the percentage of GFP-positive cells subtracted from the background (percentage of GFP-positive cells in the solvent-treated wells).

Flow cytometry

Cell suspensions were first labeled with surface fluorescent antibodies on ice for 30 min and then stained for other intracellular markers using a Cell Stimulation Cocktail (00-4975-93, eBioscience) and a Foxp3/Transcription Factor Staining Buffer Set (00-5523-00, eBioscience). Dead cells were labeled with Fixable Viability Dye eFluor 520/455UV (65-0867-14/65-0868-14, eBioscience) and excluded. The gating strategies are provided in the supplemental figures. Flow cytometry was performed on a Cytek Aurora flow cytometer, and the data were analyzed using FlowJo software (version 10.6.2).

Immunoblotting

Total protein was extracted from the cells by RIPA buffer supplemented with a cocktail of protease and phosphatase inhibitors (HY-K0010/HY-K0021/HY-K0022, MedChem Express) and quantified using a BCA kit (P0010, Beyotime). Equal amounts of proteins were loaded into the wells of SDS–PAGE gels. After electrophoresis, proteins were transferred to polyvinylidene fluoride (PVDF) membranes. After blocking, membranes were incubated with the indicated primary antibodies and HRP-conjugated secondary antibodies (1:10000, 5220-0336/5220-0341, SeraCare). The bands were obtained by chemiluminescence using Clarity Western ECL Substrate (Bio-Rad).

Immunofluorescence

For paraffin-embedded tissues, graded series of xylene and ethanol were used for dewaxing and hydration. The sections were then subjected to heat-induced antigen retrieval in sodium citrate buffer (P0081, Beyotime) using a microwave. For frozen-sectioned

Please cite this article in press as: Zhong et al., Distinct roles of TREM2 in central nervous system cancers and peripheral cancers, Cancer Cell (2024), https://doi.org/10.1016/j.ccell.2024.05.001

tissues, the sections were first incubated in PBS and restored to room temperature. The sections were then blocked with 5% donkey serum and incubated with primary antibody overnight at 4°C and fluorescence secondary antibody (Invitrogen) for 1 h at room temperature. Nuclei were stained with 4′,6-diamidino-2-phenylindole (DAPI). Fluorescent signals were detected using an Olympus FV3000 confocal microscope or an Olympus BX63 microscope.

QUANTIFICATION AND STATISTICAL ANALYSIS

Statistical tests were carried out using GraphPad Prism (version 9.5.0) software unless otherwise specified. Experimental data are presented as the mean ± standard deviation (SD) of at least three biologically independent replicates. For comparing parametric data, a two-tailed unpaired Student's t test was used to determine statistical significance. For comparing parametric data between paired tumoral and peritumoral tissues, a two-tailed paired Student's t test was used. For determining the significance of differences in survival analysis, the log rank test was applied. A p value less than 0.05 was considered statistically significant.